

1 **Skill assessment of global, regional and coastal circulation forecast models:
2 evaluating the benefits of dynamical downscaling in IBI surface waters.**

3 **Pablo Lorente¹, Marcos García-Sotillo¹, Arancha Amo-Baladrón¹, Roland Aznar¹, Bruno
4 Levier², José Carlos Sánchez-Garrido³, Simone Sammartino³, Álvaro De Pascual¹,
5 Guillaume Reffray², Cristina Toledano¹ and Enrique Álvarez-Fanjul¹**

6 [1]{Puertos del Estado, Madrid, Spain}

7 [2]{Mercator Ocean, Toulouse, France}

8 [3]{Physical Oceanography Group of University of Málaga (GOFIMA), Málaga, Spain}

9
10 Correspondence to: P. Lorente (plorente@puertos.es)

11
12 **Abstract**

13 In this work, a multi-parameter inter-comparison of diverse ocean forecast models was
14 conducted at the sea surface, ranging from global to local scales in a two-phase stepwise
15 strategy. Firstly, a comparison of CMEMS-GLOBAL and the nested CMEMS-IBI regional
16 system was performed against satellite-derived and in situ observations. Results highlighted the
17 overall benefits of both the GLOBAL direct data assimilation in open-waters and the increased
18 horizontal resolution of IBI in coastal areas, respectively. Besides, IBI proved to capture shelf
19 dynamics by better representing the horizontal extent and strength of a river freshwater plume,
20 according to the results derived from the validation against in situ observations from a buoy
21 moored in NW Spain. Secondly, a multi-model inter-comparison exercise for 2017 was
22 performed in the Strait of Gibraltar among GLOBAL, IBI and SAMPA high-resolution coastal
23 forecast system (partially nested to IBI) in order to elucidate the accuracy of each system to
24 characterize the Atlantic Jet (AJ) inflow dynamic. A quantitative validation against High
25 Frequency radar (HFR) hourly currents highlighted both the steady improvement in AJ
26 representation in terms of speed and direction when zooming from global to coastal scales
27 though a multi-nesting model approach and also the relevance of a variety of factors at local
28 scale such as a refined horizontal resolution, a tailored bathymetry and a higher spatio-temporal
29 resolution of the atmospheric forcing. The ability of each model to reproduce a 2-day quasi-
30 permanent full reversal of the AJ surface inflow was examined in terms of wind-induced
31 circulation patterns. SAMPA appeared to better reproduce the reversal events detected with
32 HFR estimations, demonstrating the added value of imposing accurate meteorologically-driven
33 barotropic velocities in the open boundaries (imported from NIVMAR storm surge model) to
34 take into account the remote effect of the atmospheric forcing over the entire Mediterranean
35 basin, which was not included in IBI and GLOBAL systems. Finally, SAMPA coastal model
36 outputs were also qualitatively analysed in the Western Alboran Sea to put in a broader
37 perspective the context of the onset, development and end of such flow reversal episodes.

38
39
40 **Keywords:** forecasting; model; inter-comparison; validation, downscaling; HF radar; skill
41 assessment;

42

1 **1 Introduction**

2 Over the last three decades, significant progresses have been made in the discipline of
3 operational oceanography thanks to the substantial increase in high-performance computational
4 resources, which has fostered the seamless evolution in ocean modelling techniques and
5 numerical efficiency (Cotelo et al., 2017) and given rise to an inventory of operational ocean
6 forecasting systems (OOFSs) running in overlapping regions in order to reliably portray and
7 predict the ocean state and its variability at diverse spatio-temporal scales.

8 Global circulation models have been steadily evolving in terms of complexity, horizontal
9 resolution refinement and process parameterisation (Holt et al., 2017). Notwithstanding, such
10 development involves compromises of scale and is subject to practical limits on the feasible
11 spatial resolution (Greenberg et al., 2007). Although large-scale physical processes are properly
12 resolved by the current state-of-the-art global models resolution (e.g. nominal 1/12°), coastal
13 and shelf phenomena are still poorly replicated or even misrepresented as the grid mesh is too
14 coarse. This is especially true for complex-geometry regions such as sea straits, archipelagos or
15 semi-enclosed seas where the coastline, seamounts and bottom topography are not well
16 resolved. In this context, tides, vertical coordinates, mixing schemes, river inflows and
17 atmospheric forcings have been traditionally identified as five areas of further research in global
18 ocean modelling (Holt et al., 2017).

19 Since the continental shelf is affected not only by natural agents (land-sea breezes, riverine
20 discharges, bottom topography, coastline shape, etc.) but also by human-induced factors, an
21 increased understanding of coastal circulation is essential for decision- and policy-making in
22 the socioeconomically vital and often environmentally stressed coastal regions. Therefore,
23 small-scale ocean features must be explicitly computed and accurately reproduced by means of
24 regional models with finer horizontal grid spacing but for a particular delimited area. The
25 success of this approach requires the seamless progress in several aspects, as previously
26 identified by Wilkin et al. (2017) and Kourafalou et al. (2015): i) a deep comprehension of the
27 primary mechanisms driving coastal circulation; ii) downscaling methods to adequately
28 represent air-sea and land-sea interactions; iii) robust methods to embed high-resolution models
29 in coarser-scale systems. Therefore, this approach implies the transfer of large-scale
30 information from the global model to the interior of the nested regional domain by means of
31 diverse methodologies. One of them is the so-called ‘spectral nudging’ technique, adopted to
32 ensure that the prevailing global conditions are not degraded in the open-ocean, while allowing
33 sub-mesoscale processes to be resolved exclusively by the nested model in the continental shelf
34 and coastal areas (Herbert et al., 2014). An alternative approach to computational time-
35 demanding multiple nesting procedures consists of using unique unstructured grid models as
36 they have been proved to properly describe ocean processes at different spatial scales (Ferrarin
37 et al., 2019; Federico et al., 2017; Ferrarin et al., 2013; Cucco et al., 2012). They benefit from
38 imposing higher resolution in shallow water areas to better resolve irregular coastlines, intricate
39 bathymetries and hence small-scale dynamics while applying a coarser grid resolution in open
40 waters to reproduce large-scale phenomena. Besides, unstructured grid models are particularly
41 effective to achieve the seamless transition between adjoining basins interconnected by narrow
42 straits (Ferrarin et al., 2018; Stanev et al., 2017; Zhang et al., 2016).

43 Additionally, the regional modelling strategy can include some fine-tuning of physical
44 parameters, individually tailored to each chosen area, instead of the universally valid
45 parameterizations associated with global OOFSs. The benefits of regional modelling over the
46 driving global OOFS are generally assumed, but to date only few studies have explored and
47 quantified the potential added value of such approach (Katavouta and Thomson, 2016; Rockel,

1 2015; Greenberg et al., 2007). The ‘parent-son’ model inter-comparison is mandatory during
2 both implementation and operational stages since it aids to: i) verify the most adequate nesting
3 strategy; ii) check the consistency of the nested model solution; and iii) identify any potential
4 problem that might be inherited from the coarser system.

5 In the framework of the Copernicus Marine Environment Monitoring Service (CMEMS), a
6 global ocean model together with a wealth of nested regional OOFSSs are currently running in
7 different areas of the European seas and providing paramount oceanographic forecast products
8 (Le Traon et al., 2018). Since the validation of OOFSSs against independent measurements
9 constitutes a core activity in oceanographic operational centres, the skill of Iberia-Biscay-
10 Ireland (IBI) regional OOFSS is routinely assessed by means of the NARVAL (North Atlantic
11 Regional VALidation) system (Sotillo et al. 2015), a web-based toolbox that provides a series
12 of skill metrics automatically computed and delivered in the QUality Information Document -
13 QUID - (Sotillo et al., 2014). In this context, the first goal of this paper is to conduct a multi-
14 parameter model inter-comparison between IBI regional OOFSS and the coarser parent system,
15 the CMEMS GLOBAL (Lellouche et al., 2018), with the aim of assessing their performance at
16 the upper-layer. Their predictive skills to properly represent the surface temperature (SST) over
17 IBI coverage domain and diverse sub-regions were evaluated by means of comparisons against
18 remote-sensed and in situ observations. On the other hand, their prognostic capabilities to
19 accurately reproduce the coastal surface circulation were assessed through the analysis of a
20 single impulsive-type river outflow episode that took place in March 2018 in the Galician coast
21 (NW Spain), a region of freshwater influence -ROFI- (Simpson, 1997).

22 Despite the recent advances in the development of CMEMS global and regional core
23 products, many downstream services for user uptake require information on even smaller spatial
24 scale, such as ocean forecasting for small island chains (Caldeira et al., 2016), intricate bights
25 (Stanev et al., 2016) or port approach areas where sharp topo-bathymetric gradients pose special
26 difficulties for accurate local predictions (Hlevca et al., 2018; Federico et al., 2017; Sánchez-
27 Arcilla et al., 2016; Sammartino et al., 2014; Grifoll et al., 2012). A variety of operational
28 products for harbours have been recently developed, although most of these coastal applications
29 are wave and water-level forecasting systems (Lin et al., 2008; Pérez et al., 2013). By contrast,
30 less attention has been devoted to harbour hydrodynamic conditions since its reduced
31 dimensions and intricate layout confer upon harbour restrictions, which are not present in the
32 open sea. Besides, derivative products based on current forecasts, such as float trajectories,
33 residence time maps, flushing patterns and risk assessment of water quality degradation can
34 constitute additional assets for efficient harbour management (Álvarez-Fanjul et al., 2018;
35 Sammartino et al., 2018). In order to overcome the existing gap between the scales effectively
36 solved by the regional OOFSSs and the coastal scales required to meet strong societal needs in
37 support of blue and green growth, a number of downstream services are currently adopting
38 different downscaling approaches. Dynamical downscaling takes regional boundary conditions
39 to drive a high-resolution limited-area model in which coastal processes are calculated on a
40 finer grid by resolving well-known hydrodynamic equations. However, uncertainties in the
41 downscaling process must be evaluated since coastal models performance can be directly
42 impacted by the propagation of any potential issue in the large-scale dynamics, inherited from
43 the coarser system (Hernández et al., 2018).

44 As a representative example of downstream service developed by Puertos del Estado (PdE)
45 in a hot spot area like the Strait of Gibraltar (GIBST), the operational PdE-SAMPA high-
46 resolution coastal system (Sánchez-Garrido et al., 2013) is partially embedded in IBI and
47 nowadays employed by the Port Authority of Algeciras Bay as predictive tool to support
48 maritime policy and assist high-stakes decision-making related to marine safety, port operation

1 optimization and mitigation of both natural disasters and anthropogenic hazards. Previous
2 research has unequivocally proved the ability of PdE-SAMPA to accurately capture basic
3 circulation features of the GIBST area and Algeciras Bay (Sanchez-Garrido et al., 2014;
4 Sammartino et al., 2014; Soto-Navarro et al., 2016). A preliminary model skill assessment was
5 conducted within the framework of MEDESS-4MS project (Sotillo et al., 2016-a). However,
6 the added value of this coastal OOFs with respect to the regional IBI system was only quantified
7 from a lagrangian perspective by using a wealth of drifters. The second goal of this contribution
8 is thus to build up upon previous model inter-comparison exercises, placing special emphasis
9 on the characterization of the Atlantic Jet (AJ) inflow into the Mediterranean Sea in terms of
10 speed and direction. This geostrophically adjusted jet fluctuates in a wide range of temporal
11 scales and drives the main circulation in the Alboran Sea, feeding and surrounding the Western
12 Alboran Gyre -WAG- (Macias et al., 2016). An inter-comparison exercise was conducted for
13 2017 among a global configuration (CMEMS GLOBAL), a regional application (CMEMS IBI)
14 and a higher resolution coastal system (PdE-SAMPA), in order to characterize the AJ dynamics
15 and their ability to adequately capture an extreme event: the quasi-permanent (up to ~48 h long)
16 full reversal of the AJ surface flow under intense and prolonged easterlies. To this end, a High-
17 Frequency radar (HFR) has been used as benchmark since it regularly provides quality-
18 controlled hourly maps of the surface currents of the Strait (Lorente et al., 2014). A detailed
19 characterization of this unusual phenomenon is relevant from diverse aspects, encompassing
20 search and rescue operations (to adequately expand westwards the search area), the
21 management of accidental marine pollution episodes (to establish alternative contingency
22 plans), or safe ship routing (to maximize fuel efficiency).

23 In summary, this paper serves one primary purpose: performing a multi-parameter model
24 skill assessment in IBI surface waters, ranging from global to local scales in a two-phase
25 stepwise strategy: i) a comparison between GLOBAL and IBI regional systems in the entire
26 overlapping coverage domain, posing special attention on regionalization; and ii) an event-
27 oriented multi-model inter-comparison for 2017 with a focus on the complete inversion of the
28 surface flow in the GIBST. This process-based validation approach, albeit commonly used in
29 meteorology and weather forecasting, is rather novel in operational oceanography and mostly
30 devoted to extreme sea level and wave height episodes.

31 This paper is organized as follows: Section 2 provides further details about the study areas.
32 Section 3 describes the diverse models configuration. Section 4 outlines the observational data
33 sources and methodology used in this study. Sections 5 and 6 present a detailed discussion of
34 the results. Finally, main conclusions are summarized in Section 7.

35

36 **2 Study Areas**

37 **2.1 IBI area (and subregions)**

38 From a pure physical oceanographic point of view, the IBI geographical domain is a very
39 complex region (Figure 1, a), marked by a generally steep slope separating the deep ocean from
40 the shelf. The western, and deeper, side of the IBI domain is affected by main large-scale
41 currents, mainly the closure of the North Atlantic Drift, here split into two major branches, the
42 major one continuing northwards along the north-western European shelves (NAC and NADC)
43 and the other, the Azores Current (AC), which follows south-eastwards and has continuity in
44 the Canary Current (CaC). On the other hand, along the slope, a poleward slope current flows
45 in the subsurface; it is observed as far north as at Ireland latitudes. Instabilities in this slope
46 current favour the occurrence of slope water oceanic eddies, along the northern Iberian coast
47 (Pingree & Le Cann 1992). On the continental shelves, intense tidal motions provide the

1 dominant source of energy (Álvarez-Fanjul et al. 1997): noticeable tidal mixing fronts arise on
2 the most energetic tidal areas of the IBI region (i.e. English Channel, Celtic and Irish Sea). Shelf
3 and coastal areas of the region are also affected by strong storm surges (Pérez et al. 2012).
4 Along the western Iberian and African coasts, strong summer upwelling of bottom cold and
5 enriched waters take place under predominant northerly wind conditions that trigger the
6 Ekman-driven offshore deflection of the surface flux.

7 IBI is also a rather broad and heterogeneous area. In order to gain insight into the model skill
8 assessment (as later exposed in Section 5), IBI service (IBISR) regional domain has been split
9 in nine different subregions (Figure 1-a): the Irish Sea (IRISH), the English Channel (ECHAN),
10 the Gulf of Biscay (GOBIS), the North Iberian Shelf (NIBSH), the West Iberian Shelf
11 (WIBSH), the Western Mediterranean Sea (WSMED), the Gulf of Cadiz (CADIZ), the Strait
12 of Gibraltar (GIBST) and the Canarias Islands (ICANA).

13

14 **2.2 Strait of Gibraltar**

15 The Strait of Gibraltar (GIBST), the only connection between the semi-enclosed
16 Mediterranean basin and the open Atlantic Ocean (Figure 1, b), is characterized by a two-layer
17 baroclinic exchange which is hydraulically controlled at Camarinal Sill (Sánchez-Garrido et al.,
18 2011). Whilst saltier Mediterranean water flows out at depth, an eastward surface jet of
19 relatively fresh Atlantic water (AJ) flows into the Alboran Sea by surrounding the quasi-
20 permanent Western Anticyclonic Gyre (WAG) and the more elusive Eastern Anticyclonic Gyre
21 (EAG) in a wavelike path. As the WAG owes its existence to the input of new Atlantic waters
22 provided by the AJ, both structures are widely considered to be coupled and usually referred as
23 to the AJ-WAG system. A significant variety of analytical, field and modelling studies have
24 previously attempted to disentangle the AJ-WAG system and properly explain the underlying
25 physical processes (Sánchez-Garrido et al., 2013; Macías et al., 2007-a; Viúdez, 1997).

26 The position, intensity and direction of the AJ fluctuate in a broad range of temporal scales,
27 driving the upper-layer circulation of the Alboran Sea with subsequent physical and biological
28 implications (Solé et al, 2016; Sánchez-Garrido et al. 2015; Ruiz et al., 2013). For instance, the
29 presence of a strong AJ close to the northern shore of the Alboran Sea reinforces the coastal
30 upwelling and therefore increases both the near-shore chlorophyll concentration and the
31 spawning of fish in this region (Ruiz et al., 2013; Macías et al., 2008). By contrast,
32 meteorologically-induced inflow interruptions can trigger the weakening and even the
33 decoupling of the AJ-WAG system (Sánchez-Garrido et al., 2013), the subsequent eastward
34 migration of the WAG and the genesis of a new gyre that coexists with the other two, giving
35 rise to a three-anticyclonic-gyre situation (Viúdez et al., 1998).

36 Within this context, the AJ pattern has been described to oscillate between two main
37 circulation modes at seasonal scale (Vargas-Yáñez et al., 2002): i) a stronger AJ flows north-
38 eastwards during the first half of the year and ii) a weaker AJ flows more southwardly towards
39 the end of the year. Sea level Pressure (SLP) variations over the Western Mediterranean basin
40 and local zonal wind (U) fluctuations in the Alboran Sea have been usually considered as the
41 main factors controlling and modulating the AJ variability (Macías et al., 2007-b; Lafuente et
42 al., 2002). In particular, the second parameter has been largely invoked as the primary driving
43 agent to explain both the intensification of the surface inflow during prevalent westerlies and
44 also extreme AJ collapse events recorded when intense easterlies are predominant (Macías et
45 al., 2016). The zonal wind intensity has been reported to follow an annual cycle with more
46 westerly (easterly) winds during winter (summer) months (Dorman et al., 1995). The seasonal
47 variability and occasional interruptions of the Atlantic inflow due to meteorological forcing

1 have been earlier investigated with in situ data from fixed moorings (García-Lafuente, 2002).
2 More recently, a considerable number of satellite tracked drifters were released on both sides
3 of GIBST within the framework of MEDESS-4MS project, providing hence a complete
4 Lagrangian view of the Atlantic waters inflow into the Alboran Sea (Sotillo et al., 2016-b).

5

6 **3 Models description**

7 Whereas basic features of the three OOFSSs employed in this work are gathered in Table 1,
8 further details are provided in the following devoted sub-sections.

9 **3.1 CMEMS GLOBAL system**

10 The Operational Mercator global ocean analysis and forecast system provides 10 days of 3D
11 global ocean forecasts updated daily. This product includes daily mean files of temperature,
12 salinity, currents, sea level, mixed layer depth and ice parameters from the surface to seafloor
13 over the global ocean. It also includes hourly mean surface fields for sea level height,
14 temperature and currents. The global ocean output files are displayed with a 1/12 degree
15 horizontal resolution with regular longitude/latitude equirectangular projection. 50 vertical
16 levels span from 0 to 5500 meters.

17 The product is updated as follows: everyday, the daily configuration is run with updated
18 atmospheric forcings, without assimilation, for days D-1 to D+9. The daily runs are initialized
19 with the previous day's run, except on Thursdays, when they start from the weekly analysis run.
20 Every week, on Wednesdays, the weekly configuration is run with assimilation for days D-14
21 to D-1. This run is separated in two parts: a best analysis for days D-14 to D-8 and an analysis
22 for days D-7 to D-1. Therefore, every day, the time series is updated with new forecasts for
23 days D-1 to D+9, erasing the previously available data for D-1 to D+8. In addition, on
24 Thursdays, the analysis is also provided, replacing previously available files for days D-14 to
25 D-1. For further details, the reader is referred to the GLOBAL Product User Manual -PUM-
26 (Law Chune et al., 2019).

27 The system is based on the Nucleus for European Modelling of the Ocean (NEMO) v3.1
28 ocean model (Madec, 2008). The physical configuration is based on the tripolar ORCA grid
29 type with a horizontal resolution of 9 km at the equator, 7 km at Cape Hatteras (mid-latitudes)
30 and 2 km toward the Ross and Weddell seas. The 50-level vertical discretization retained for
31 this system has 1 m resolution at the surface decreasing to 450 m at the bottom, and 22 levels
32 within the upper 100 m. The bathymetry used in the system is a combination of interpolated
33 ETOPO1 and GEBCO8 databases. The system was initialized on 11 October 2006 based on the
34 temperature and salinity profiles from the EN4 monthly gridded climatology. The atmospheric
35 fields forcing the ocean model are taken from the ECMWF (European Centre for Medium-
36 Range Weather Forecasts) Integrated Forecast System. A 3-h sampling is used to reproduce the
37 diurnal cycle. The system does not include neither tides nor pressure forcing. The monthly
38 runoff climatology is built with data on coastal runoffs and 100 major rivers from the Dai et al
39 (2009) database (Lellouche et al., 2018). Altimeter data, in situ temperature and salinity vertical
40 profiles and satellite sea surface temperature are jointly assimilated to estimate the initial
41 conditions for numerical ocean forecasting. Moreover, satellite sea ice concentration is now
42 assimilated in the system in a monovariate/monodata mode. More information can be found in
43 Lellouche et al., (2018).

1 **3.2 CMEMS IBI regional system**

2 The IBI OOFS provides a real-time short-term 5-day hydrodynamic 3D forecast (and one
3 day of hindcast as best estimate) of a range of physical parameters (currents, temperature,
4 salinity and sea level) since 2011 (Sotillo et al., 2015). IBI is based on an eddy-resolving NEMO
5 model application (v3.6) that includes high-frequency processes required to characterize
6 regional-scale marine processes. The model application is run at 1/36° horizontal resolution and
7 final products are routinely delivered in a service domain extending between 19°W-5°E and
8 26°N-56°N. The NEMO model (Madec, 2008) solves the three-dimensional finite-difference
9 primitive equations in spherical coordinates discretized on an Arakawa-C grid and 50
10 geopotential vertical levels (z coordinate), assuming hydrostatic equilibrium and Boussinesq
11 approximation. Partial bottom cell representation of the bathymetry (a composite of ETOPO 2
12 and GEBCO8) allows an accurate representation of the steep slopes characteristic of the area.
13 The model grid is a subset of the Global 1/12° ORCA tripolar grid used by the parent system
14 (the CMEMS GLOBAL system) that provides initial and lateral boundary conditions, but
15 refined at 1/36° horizontal resolution.

16 The IBI run is forced every 3 hours with up-to-date high-frequency (1/8° horizontal grid
17 resolution) meteorological forecasts (10-m wind, surface pressure, 2-m temperature, relative
18 humidity, precipitations, shortwave and longwave radiative fluxes) provided by ECMWF.
19 CORE empirical bulk formulae (Large and Yeager, 2004) are used to compute latent sensible
20 heat fluxes, evaporation and surface stress. Lateral open boundary data are interpolated from
21 the daily outputs of the GLOBAL system. These are complemented by 11 tidal harmonics built
22 from FES2004 (Lyard et al., 2006) and TPXO7.1 (Egbert and Erofeeva, 2002) tidal models
23 solutions. Fresh water river discharge inputs are implemented as lateral open boundary
24 condition for 33 rivers. Flow rate data imposed is based on a combination of daily observations
25 from PREVIMER, simulated data from E-HYPE hydrological model and monthly
26 climatological data from GRDC and French “Banque Hydro” dataset. Further details can be
27 found in Sotillo et al., (2015).

28 Originally, the operational IBI system was based on a periodic re-initialization from the
29 GLOBAL parent solution. Afterwards, IBI has steadily evolved: by April 2016, an upgrade of
30 the downscaling methodology was implemented, substituting the periodic re-initialization by a
31 spectral nudging technique in order to avoid temporal discontinuity inherent to the periodic re-
32 initialization and minimize dependency from the GLOBAL parent solution on the shelf.

33 The spectral nudging aims at forcing the regional child model solution (IBI) to be close to
34 the parent system (GLOBAL) in those areas where the latter is supposed to be accurate thanks
35 to data assimilation, mainly in deep waters outside the continental shelf (Herbert et al., 2014).
36 After each forecast cycle of IBI, the increment between the parent model analysis X_p and the
37 child model forecast X_c is calculated for a chosen state variable X (typically currents,
38 temperature and salinity). Such increment consists of a space and time low pass filter of the
39 differences $X_p - X_c$ in order to keep the characteristic scales the parent GLOBAL system can
40 properly resolve (from large-scale to mesoscale). After each forecast cycle of the child IBI
41 system, a new cycle (called analysis) is re-launched where X_c is nudged to X_p at each time step
42 by the weekly mean of the daily increments previously computed in the parent system grid
43 during the forecast cycle. The 1-week time smoothing window was imposed as this is the typical
44 timescale associated with mesoscale structures.

45 Furthermore, the nudging is spatially limited in those areas where the parent system can not
46 improve the regional model (e.g. where there is no data assimilation of altimetry or where the
47 physics is missing, for instance on the shelf) or where the spatial filtering processes are

1 potentially detrimental (close to the bottom or the open boundaries). This spatial weight
2 function is a 3D mask (for further details, see Herbert et al., 2014) that differentiates the zones
3 where IBI system is nudged and thus reconciled with the parent system (typically in the open
4 sea) from those where IBI remains free (continental shelf, coastal areas and regions close to the
5 open boundaries) to fully compute higher frequency processes such as thermal tidal fronts, river
6 discharges, etc.

7 Finally, a SAM2-based data assimilation scheme (Lellouche et al., 2013; Brasseur et al.,
8 2005) was recently introduced (April 2018) in order to enhance IBI predictive skills but will
9 not be further described here as only outputs from 2017 have been used in the present work.

10 **3.3 PdE SAMPA coastal system**

11 The PdE-SAMPA operational forecast service started in April 2012 (Sammartino et al.,
12 2014; Sánchez-Garrido et al., 2014). It routinely provides a daily short-term forecast (72-h
13 horizon) of currents and other oceanographic variables in the Gibraltar Strait and its
14 surroundings (Gulf of Cadiz and Alboran Sea). The PdE-SAMPA model application was
15 developed by the University of Malaga in collaboration with PdE in order to provide a tailored
16 forecasting service to one of their main stakeholders, the harbor of Algeciras Bay (Figure 1-
17 b). It is based on the Massachusetts Institute of Technology global circulation model -MITgcm-
18 (Marshall et al., 1997). The domain, which extends from the Gulf of Cádiz to the Alboran Sea
19 (Figure 1-b), is discretized with an orthonormal curvilinear grid of variable horizontal
20 resolution, sparser close to the boundaries (~ 8-10 km) and higher in the Strait (~ 300-500 m).
21 In the vertical dimension, SAMPA has 46 unevenly spaced z levels with maximum resolution
22 of 5 m near the surface, exponentially decaying towards the seafloor. The shallower level is at
23 2.5 m depth. The bathymetry is derived from a combination of the GEBCO bathymetry data set
24 and fine-resolution bathymetric charts of the Strait of Gibraltar and the continental shelf of the
25 Gulf of Cadiz and northern coast of the Alboran Sea. The bottom topography is represented as
26 partial vertical cells. In the two lateral open boundaries (west and east) the model is partially
27 forced by daily mean temperature, salinity and velocity fields from CMEMS-IBI regional
28 model (Sotillo et al., 2015). Since such frequency is not suitable to resolve barotropic flows
29 through the Strait either (García-Lafuente et al. 2002), tidal and meteorologically-driven
30 barotropic velocities are prescribed across the open boundaries: the former extracted from the
31 Mog2d model described by Carrere and Lyard (2003) and the latter from the storm surge
32 operational system developed by Álvarez-Fanjul et al. (2001), which accounts for the remote
33 effect of the atmospheric forcing in the barotropic flow through GIBST. This nesting strategy
34 ensures that the SAMPA model captures a realistic variability of inflow and outflow currents
35 through the Strait. At the sea surface, the model is forced by hourly values of wind stress, air
36 humidity and temperature, fresh water and heat surface fluxes provided by the Spanish
37 Meteorological Agency through the operational Forecast System based on the HIRLAM model
38 (Cats, G.; Wolters, 1996). Further details on the SAMPA model configuration are provided in
39 Sanchez-Garrido et al. (2013).

40 **4 Validation of OOFSS**

41 **4.1 Framework**

42 The validation of OOFSSs against independent measurements constitutes a core activity in
43 oceanographic operational centres since it aids: i) to infer the relative strengths and weaknesses
44 in the modelling of several key physical processes; ii) to compare different versions of the same
45 OOFSS and evaluate potential improvements and degradations before a new version is
46

1 transitioned into operational status; iii) to compare coarse resolution ‘father’ and nested high-
2 resolution ‘son’ systems to quantify the added value of downscaling.

3 With regards to the third aspect, IBI forecast products are regularly intercompared not only
4 against other CMEMS regional model solutions (e.g. NWS and MED) in the overlapping areas
5 but also against its parent system (GLOBAL) by means of NARVAL (North Atlantic Regional
6 VALidation) login-protected web-based application (Sotillo et al. 2015). This tool has been
7 implemented to routinely monitor IBI performance and to objectively inter-compare models’
8 reliability and prognostic capabilities. Both real-time validation (‘online mode’) and regular-
9 scheduled ‘delayed-mode’ validation (for longer time periods) are performed using a wealth of
10 observational sources as benchmark, among others: in situ observations from buoys and tide-
11 gauges, SST satellite derived products, temperature and salinity profiles from ARGO floats and
12 HFR. Product quality indicators and skill metrics are automatically computed in order to infer
13 IBI accuracy and the spatiotemporal uncertainty levels. The evaluation metrics regularly
14 generated by NARVAL are online delivered in the QUID, which is periodically updated and
15 freely available in CMEMS website (<http://marine.copernicus.eu/>).

16 Complementarily, opportunistic inter-comparisons are conducted in the frame of diverse
17 EU-funded projects such as MEDESS-4MS (Sotillo et al., 2016-a): 35 satellite tracked drifters
18 were released on both sides of the Strait of Gibraltar and the quality-controlled in situ data of
19 sea surface temperature and currents were collected to build the MEDESS-GIB database
20 (Sotillo et al., 2016-b), providing hence a complete Lagrangian view of the surface inflow of
21 Atlantic waters through the GIBST and the Alboran Sea. Such valuable oceanographic
22 information was subsequently used to intercompare IBI and SAMPA forecast products to
23 identify strengths (realistic simulation of the Atlantic Jet and the Algerian Current) and
24 shortcomings (position and intensity of the Alboran gyres, especially the western one) in both
25 models performance. This exercise reflected the effectiveness of the dynamical downscaling
26 performed through the SAMPA system with respect to the regional solution (in which SAMPA
27 is partially nested, as it is also embedded in Mog2D and NIVMAR models), providing an
28 objective measure of the potential added value introduced by SAMPA.

29 Eventually, ancillary validation approaches have been recently adopted focused on the
30 evaluation of ocean models performance in specific situations and on their ability to accurately
31 reproduce singular oceanographic processes (Hernández et al., 2018). Since the NARVAL tool
32 is devoted to inter-compare model solutions on a monthly, seasonal or annual basis, part of the
33 picture is missing due to traditional time averaging. Hence the quality indicators computed,
34 albeit valid, mask somehow models’ capabilities to replicate ocean phenomena of particular
35 interest at shorter timescales. This event-oriented multi-model inter-comparison methodology
36 allows to better infer the ability of each system to capture small-scale coastal processes. In this
37 context, the recurrent question “*Which model is the best one?*” should be reformulated by firstly
38 admitting that one system can outperform the rest of OOFs for a particular event but by contrast
39 can be also beaten when attempting to reproduce and characterize some other distinct ocean
40 phenomenon.

41 Those oceanographic events subject of further insight might encompass, among others: i) coastal upwelling, dowelling and relaxation episodes; ii) submesoscales eddies (Mourre et al.,
42 2018); iii) extreme events; iv) complete flow reversals. Particularly, in the present work the
43 attention has been devoted to the full and permanent reversal of the surface AJ in the GIBST
44 during, at least, 48 hours. This unusual episode has been detected by means of HFR current
45 estimations and further examined with OOFs outcomes. The agreement between both in situ
46 and remote-sensing instruments and the ocean forecasting system has been evaluated by means
47

1 of computation of a set of statistical metrics traditionally employed in this framework:
2 histograms, bias, root mean squared differences (RMSD), scalar and complex correlation
3 coefficients, current roses, histograms, quantile-quantile (QQ) plots and the best linear fit of
4 scatterplots. In the following sub-section all the in situ and remote-sensed observations
5 employed in the present work are described.

6 **4.2 Observational data sources**

7 ***In situ observations***

8 The study domain includes an array of buoys operated by Puertos del Estado and the Irish
9 Marine Institute (Figure 1, a), providing quality-controlled hourly-averaged observations of
10 SST, SSS and currents. To ensure the continuity of the data record, occasional gaps detected in
11 time series (not larger than 6 hours) were linearly interpolated. Basic features of each in-situ
12 instrument are described in Table 2.

13 ***Satellite-derived observations***

14 The European Ocean Sea Surface Temperature L3 Observations is a CMEMS operational
15 product which provides a daily fusion of SST measurements from multiple satellite sensors
16 over a 0.02° resolution grid. The L3 multi-sensor (supercollated) product is built from bias-
17 corrected L3 mono-sensor (collated) products. If the native collated resolution is N and $N < 0.02^{\circ}$ the change (degradation) of resolution is done by averaging the best quality data. If $N > 0.02^{\circ}$ the collated data are associated to the nearest neighbour without interpolation nor artificial
18 increase of the resolution. A synthesis of the bias-corrected L3 mono-sensor (collated) files
19 remapped at resolution R is done through a selection of data based on the following hierarchy:
20 AVHRR_METOP_B, SEVIRI, VIIRS_NPP, AVHRR-19, AVHRR-18, MODIS_A,
21 MODIS_T, AMSR2. This hierarchy can be changed in time depending on the health of each
22 sensor. Further details can be found in the Product User Manual (PUM), freely available in
23 CMEMS website (<http://cmems-resources.cls.fr/documents/PUM/CMEMS-SST-PUM-010-009.pdf>)

27 ***HFR-derived observations***

28 The HFR system employed in the present study consists of three-site shore-based CODAR
29 Seasonde network, installed in GIBST (Fig 1, b-c). Hereafter the sites will be referred to by
30 their four letter site codes: CEUT, CARN, and TARI, respectively (Figure 1, c). Each site is
31 operating at a central frequency of 26.8 MHz, providing hourly radial current measurements
32 which are representative of the upper 0.5 m of the water column. The maximum horizontal
33 range and angular resolution are 40 km and 5° , respectively. Radial current measurements from
34 the three stations are geometrically combined with an averaging radius set to 3 km, in order to
35 estimate hourly total current vectors on a Cartesian regular grid of 1x1 km horizontal resolution.

36 A source of error to be considered in the computation of the total vectors is the so-called
37 Geometrical Dilution of Precision (GDOP). The GDOP is defined as a dimensionless
38 coefficient of uncertainty that characterizes how radar system geometry may impact on the
39 measurements accuracy and position determination errors, owing to the angle at which radial
40 vectors intersect. Maps of east and north GDOP for this HFR system (not shown) follow a
41 pattern where their values increase with the distance from the radar sites and along the baselines
42 (lines connecting two HFR sites), as the combining radial vectors are increasingly parallel and
43 the orthogonal component tends to zero. Further details can be obtained from Lorente et al.
44 (2018).

1 The accuracy of HFR measurements, which are affected by intrinsic uncertainties (radio
2 frequency interferences, environmental noise, etc.) have been previously assessed by
3 comparing against in situ observations provided by a point-wise current meter (Lorente et al.,
4 2014), yielding correlations above 0.7 and RMSD below $13 \text{ cm} \cdot \text{s}^{-1}$. Such results revealed that
5 this HFR network has been operating within tolerance ranges, properly monitoring the surface
6 circulation in near real-time of this geostrategic region.

7 Recent works relying on this HFR system have successfully investigated the water exchange
8 between Algeciras Bay and the Strait of Gibraltar (Chioua et al., 2017), the impact of the
9 atmospheric pressure fluctuations on the mesoscale water dynamics of the Strait of Gibraltar
10 and the Alboran Sea (Dastis et al., 2018), the dominant modes of spatio-temporal variability of
11 the surface circulation (Soto-Navarro et al., 2016) or the characterization of the Atlantic surface
12 inflow into the Mediterranean Sea (Lorente et al., 2018).

13 In the present work, quality-controlled hourly HFR current measurements collected during
14 the entire 2017 were used as benchmark to elucidate the skill of a number of OOFs. The data
15 availability was significantly high: almost 100% in the selected transect (solid black
16 longitudinal line, shown in Figure 1-c), decreasing in the easternmost sectors. The transect here
17 used to examine the AJ surface inflow was readily chosen as the associated total GDOP,
18 reported in Lorente et al (2018), was reduced (below 1.3) and the spatial and temporal data
19 availability were optimal during 2017. From an oceanographic perspective, the election of such
20 transect was also convenient to better characterize both the intensity and direction of the AJ,
21 since its midpoint covers the area where the highest peak of current speed is usually detected
22 and also where the inflow orientation is not influenced yet by the water exchange between
23 Algeciras Bay and the Strait of Gibraltar.

24

25 5 Comparison between CMEMS model solutions in IBI waters

26 *Temperature*

27 The CMEMS L3 satellite-derived daily data were used to validate the SST fields predicted
28 by both GLOBAL and IBI systems. The map of annual availability of this remote-sensing
29 product for 2017 (Figure 2, a) reveals that the highest percentages of available observations
30 (above 80%) were found in the south of Canary Islands, the Gulf of Cadiz and in the Western
31 Mediterranean Sea. Equally, there was also a significant data provision in the west coast of the
32 Iberian Peninsula and Morocco, although it decreased to 70% in nearshore areas over the shelf
33 such as the Iberian and African upwelling or the Strait of Gibraltar. By contrast, the lowest data
34 availability (below 40%) was detected in the northernmost latitudes, including the Irish and
35 North Seas.

36 Maps of annual Mean Absolute Differences (MAD) were firstly computed in open waters
37 where the spectral nudging technique was applied (Figure 2, b-c). Apparently, both models
38 behaved similarly during 2017, although GLOBAL performance was slightly better due to the
39 direct data assimilation scheme implemented, as reflected by a lower spatially-averaged MAD
40 of 0.13° . In the open sea, IBI benefited indirectly from the data assimilation conducted in its
41 parent system thanks to the spectral nudging technique ($\text{MAD} = 0.15^\circ$), allowing thereby the
42 regional and global model states to be reconciled with each other. IBI even outperformed
43 GLOBAL locally in specific zones (delimited with blue rectangles in Figure 2-b) such as the
44 western Canary Islands, the periphery of Madeira Island or a portion of the African coastal
45 upwelling system. Furthermore, a narrow belt of SST anomalies could be observed along the
46 continental shelf break in the case of GLOBAL (Figure 2, b). Since IBI presents a higher grid

1 resolution, it could partially resolve the internal waves breaking which leads to turbulence and
2 energy for increased vertical mixing with cooler waters beneath the pycnocline, ultimately
3 contributing to the reduced SST differences observed in IBI estimations over the continental
4 shelf break (Figure 2, c). By contrast, GLOBAL appeared to outperform IBI in the Gulf of
5 Cadiz, the NW Iberian open waters and the region comprised between Canary and Madeira
6 Islands (Figure 2, c).

7 Maps of annual MAD in coastal areas (Figure 2, d-e), where no spectral nudging was
8 imposed and IBI system run freely, exhibited some similarities such as the pronounced SST
9 differences encountered in the Iberian and African Coastal Upwelling Systems (ICUS and
10 ACUS hereinafter, respectively). According to the skill metrics, spatially-averaged over the
11 entire coastal waters domain, IBI performance was, on average, more accurate than GLOBAL
12 one (0.17° versus 0.20°) thanks to several factors (i.e., the more refined mesh and the tidal
13 solution included in IBI). GLOBAL outputs exhibited relevant SST differences over the
14 continental shelf, especially in energetic tidally-dominated areas such as the English Channel,
15 the Irish Sea and southern part of the North Sea (Figure 2, d). In these regions, monthly maps
16 of SST bias (not shown) revealed the alternation between winter cold anomalies and summer
17 warm anomalies, in accordance with earlier results of Graham et al. (2018). Tidally driven
18 vertical mixing could account for a portion of the discrepancies encountered between the
19 coarser detided GLOBAL and IBI model solutions, where the former seems to predict an over-
20 stratification in shelf-seas. IBI also appeared to slightly outperform GLOBAL in some
21 delimited areas of the Portuguese coast, the Gulf of Cadiz and the ACUS (Figure 2, d). Besides,
22 the higher SST anomalies observed for GLOBAL in the Strait of Gibraltar and the Western
23 Alboran Sea were likely linked to the inadequate representation of the speed and direction of
24 the Atlantic Jet inflow, something that will be addressed in the following sections. On the
25 contrary, it is also true that GLOBAL was to a little extent more precise in some parts of
26 Western Mediterranean, the ICUS and ACUS (Figure 2, e).

27 The MAD metrics for each subregion within IBI regional domain (defined in Figure 1-a) are
28 shown in Figure 3. As above mentioned, IBI generally outperformed GLOBAL system in those
29 subregions where no spectral nudging was applied (English Channel, Irish and North Sea, North
30 Iberian shelf), with the exception of the Western Iberian Shelf (WIBSH). In addition, better
31 metrics were obtained for IBI in the Gulf of Biscay (GOBIS), where the spectral nudging was
32 only applied in the westernmost off-shelf area. On the contrary, GLOBAL seemed to better
33 replicate the SST field in the open sea thanks to the direct data assimilation. IBI metrics, albeit
34 consistent, were slightly worse than those obtained for GLOBAL in this region.

35 Although both models appeared to better fit to observations in the open sea, a portion of the
36 SST differences detected in this region might be attributed to the fact that the satellite data
37 assimilated into GLOBAL system (CMEMS OSTIA gap-free product) are different from the
38 independent (not-assimilated) satellite-derived observations (CMEMS L3 gappy product) used
39 as benchmark comprehensively validate the models. Furthermore, satellite products are affected
40 by intrinsic uncertainties. The Quality Information documents (QUIDS) focused on the
41 accuracy assessment of OSTIA (McLaren et al., 2016) and L3 (Saux-Pickart et al., 2019)
42 satellite products have reported a RMSD of 0.4° (0.2°) between OSTIA (L3) and drifting buoys
43 observations for 2012 (2018). More specifically, in the case of OSTIA estimations the RMSD
44 is 0.40° globally with regional values ranging from 0.28° in the South Pacific to higher values
45 in the North Atlantic (0.47°) or in the Mediterranean Sea (0.89°). By contrast, the L3 SST
46 product shows reasonably good difference statistics against drifting buoy measurements. This
47 bias in satellite estimations should be taken into account when interpreting the results of the
48 models validation.

1 On the other hand, the highest SST discrepancies for both models were generally located in
2 very coastal areas (African and Iberian upwelling systems, Strait of Gibraltar, etc.) and over the
3 continental shelf (the Irish Sea and the English Channel) where satellite remote sensing could
4 be complicated by weather patterns and dissolved organic compounds of terrestrial origin that
5 may attenuate signals and yield unreliable results (Thakur et al., 2018). As a consequence, many
6 processed remote sensing products apply a land mask that excludes mixed pixels in nearshore
7 areas, use temporal averaging to account for missing observations or even impose an optimal
8 interpolation process to transform the original satellite tracks into a regular grid (i.e., OSTIA
9 product). In this context, the availability of the SST L3 data (Figure 2, a) was lower on the shelf
10 near coastal areas featuring a complex bathymetry (likely due to poor satellite coverage,
11 application of a land mask or cloud cover), justifying to some extent the predominance of SST
12 anomalies near the shorelines.

13 For the sake of completeness, supplementary validation works in the entire 3D water column
14 with Argo-floats are regularly conducted to assess model vertical structure. For the period 2012-
15 2016 and the entire IBI domain, the averaged RMSD for full profiles of temperature and salinity
16 are 0.51° and 0.13 PSU, respectively (for further details, we refer the reader to the IBI QUID).
17 Both models perform fairly well in open-waters, given the fact that GLOBAL assimilates this
18 type of in situ observations and subsequently transfers the information to the nested IBI system
19 thanks to the aforementioned spectral nudging technique. Nevertheless, validation focused on
20 smaller scales and high frequency processes is still crucial to analyze in detail the performance
21 of both modelled products in intricate coastal regions.

22 Hourly in situ observations from eight buoys, moored within specific sub-regions (Figure 1,
23 a), were used as benchmark to validate both GLOBAL and IBI outputs. The annual time series
24 of SST exhibited a significantly high resemblance, properly reproducing the expected annual-
25 cycle shape (Figure 4). According to the consistent skill metrics derived from the comparison
26 against three deep-water buoys (B3, B4 and B5, in Table 2), both models had a rather alike
27 performance during 2017 with RMSD and correlation coefficients in the ranges [0.44-0.96] °C
28 and [0.86-0.99], respectively (Figure 4: c, d, e). While the similar behaviour observed off the
29 shelf is partially attributable to the aforementioned spectral nudging technique, the model-
30 observation comparison in near-shore areas revealed noticeable discrepancies.

31 On one hand, IBI appeared to outperform GLOBAL system in the Irish Sea (Figure 4, b),
32 Gulf of Cadiz (Figure 4, f) and GISBT sub-region (Figure 4, g), as reflected by lower (higher)
33 RMSD (correlation) values obtained. Particularly, the results for the Strait of Gibraltar are not
34 in complete accordance with the statistics previously derived from the comparison against L3
35 satellite-derived data (Figure 3, j), likely due to the fact that remote-sensed SST estimations
36 area might be affected by higher intrinsic uncertainties (i.e. land contamination and cloud
37 cover). Although both comparisons against remote and in situ observations confirmed the
38 model SST overestimation in GIBST, especially during summertime, the former (latter)
39 indicated that IBI precision was significantly lower (higher). Another relevant aspect is the
40 notable ability of IBI to capture sharp summer SST rise (steeper than 3°C) during prevalent
41 easterlies (Figure 4, g), as a result of the surface inflow reversal and subsequent intrusion of
42 warmer Mediterranean waters into GIBST (this phenomenon will be subject of further analysis
43 in Section 7). However, GLOBAL appeared to overestimate SST in this area during the entire
44 year, as reflected by a RMSD of 1.64°C.

45 On the other hand, GLOBAL seemed to behave slightly better at B1 location -IBISR area-
46 (Figure 4, a) and substantially more accurately at B8 buoy location - in the Canarias Islands,
47 ICANA-, where a permanent SST overestimation from June to December was evidenced in IBI

1 predictions (Figure 4, h), yielding thereby a RMSD twice higher than that obtained for
2 GLOBAL estimations, in agreement with Figure 2 (i-j) and Figure 3 (i). The lower performance
3 of IBI in ICANA sub-region was previously reported by Aznar et al (2016) when inter-
4 comparing IBI forecast and 1/12° reanalysed solutions. At this point it is worth recalling that
5 GLOBAL includes a data assimilation scheme, whereas IBI takes realistic ocean conditions
6 from weekly global analyses. This fact shows up the possible benefits of the observational data
7 assimilation in these areas, at least in terms of surface variables. Furthermore, a fraction of
8 observed model-buoy discrepancies in SST can be explained in terms of disparate depth scales:
9 whereas IBI and GLOBAL daily outputs are representative of the temperature in the upper one
10 meter of the water column, moored buoys provide temperature estimations at a deeper nominal
11 depth (between 1 and 3.5 m, depending on the brand). Future validation exercises should
12 include the interpolation of model outputs to both the exact buoy location and also to the
13 specific depth level in order to more accurately assess the model skilfulness. It is worthwhile
14 mentioning that a variety of previous works have focused on the comparison of in situ and
15 remote-sensed SST data, reporting significant differences across different geographical regions
16 (Thakur et al., 2018; Stobart et al., 2015; Smit et al., 2013). Such discrepancies could be also
17 observed in this work as lower biases were generally derived from the point-wise comparisons,
18 highlighting thereby the intrinsic uncertainties associated with satellite data in nearshore areas.

19 Complementarily, a quarterly analysis was performed to infer any potential degradation in
20 model performances during a specific season of the year (Figure 5). Overall, both GLOBAL
21 and IBI predictions seemed to be more reliable in winter (except at B1 location: Figure 5-a) in
22 terms of lower RMSD. They also emerged to be less realistic during summer, as denoted by
23 abrupt decreases in quarterly correlation indexes (from 0.9 down to 0.5) at B2, B4 and B6
24 locations and the relevant rise of RMSD (up to 2.5°C) at B7 location (GIBST sub-region). This
25 SST overestimation could be partially explained in terms of imprecise latent sensible heat fluxes
26 and excess of evaporation, although additional efforts should be devoted to shed light on it.
27 Once again, IBI performance appeared to be more accurate in coastal zones featuring a more
28 complex bathymetry (at B2, B4, B6 and B7 locations), whereas GLOBAL fitted better to in situ
29 observations in off shelf regions such as at B1 and B8 locations. In the rest of the cases, both
30 model solutions were rather alike. It is noteworthy that each point-wise buoy is not
31 representative of the entire sub-region in which is deployed, explaining thus to some extent the
32 discrepancies arisen between sub-sections 6.1 and 6.2.

33 ***Salinity***

34 As pointed out in the introduction, the enhancement of riverine forcing is still as a priority
35 in ocean modelling as the estuarine circulation is mainly driven by horizontal density gradients
36 which are ultimately modulated by freshwater inputs. In this context, previous works have
37 investigated the potential benefits of replacing old climatologies by data from hydrological
38 model predictions (O'Dea et al., 2017). Here we provide a specific example to illustrate the
39 discrepancies between GLOBAL and IBI performances in the Galician coast (NW Spain), as a
40 consequence of the different horizontal resolution and distinct runoff forcing implemented in
41 the operational chain. While both models performances are rather similar in open-waters
42 (according to the results derived from the validation against 3D Argo-float profiles and exposed
43 in the QUID), higher discrepancies are expected to arise in coastal and shelf areas as they are
44 governed by small-scale processes such as land-sea breezes, runoff (and the resulting
45 stratification and buoyancy-driven circulation), transport materials (nutrients, sediments,
46 pollutants, etc.).

1 As shown in Figure 6-a, hourly in situ SSS data collected by B4 buoy during March 2018
2 experienced an abrupt decrease from a standard value around 36 PSU down to almost 33 PSU
3 in just few hours during the 20th of March, likely due to a noticeable filament of freshwater
4 discharged by Miño River. IBI outputs at the closest grid point appeared to properly capture
5 both the sharp drop in SSS values and the persistent low salinity values for the next 4-day
6 period. By the end of the month, the modelled salinity field seemed to steadily recover to usual
7 levels in the range of 35.5-35.8 PSU, whereas in situ observations revealed a steeper rise to
8 34.8 PSU by the 23th of March. Nevertheless, the skill metrics confirmed the rather accurate
9 IBI performance, with a correlation coefficient of 0.92 and a RMSD of 0.33 PSU. By contrast,
10 although GLOBAL outputs could replicate the mean SSS, it did not reproduce satisfactorily the
11 freshwater episode and barely showed any temporal variability, as reflected by a negligible
12 correlation coefficient (0.09) and a higher RMSD (0.84 PSU).

13 Consequently, the impact of colder freshwater river inputs on the SST was also evaluated
14 (Figure 6, b). Once again, while the sudden cooling of 1.5°C denoted by in situ observations
15 was fairly well replicated by IBI, GLOBAL system could only correctly predict the overall
16 decreasing trend along with the SST values immediately before (13.5°C) and after (13°C) the
17 analysed event. As a consequence, the monthly correlation coefficient (RMSD) obtained for
18 IBI is higher (lower): 0.79 versus 0.20 (0.25°C versus 0.35°C). It is worth mentioning that we
19 could not find any relevant evidence that could justify that the observed SST drop was also
20 partially attributable to a large-scale process (i.e., coastal upwelling event). The wind rose
21 (derived from B4 buoy observations) and map of HFR-derived surface currents for May 2018
22 (not shown) did not exhibit the well-documented conditions associated with NW Iberian
23 upwelling episodes, such as the predominant northerly winds and the subsequent offshore
24 deflection of the surface flux, respectively.

25 The buoyancy input introduced by large freshwaters fluxes (particularly during the spring
26 freshet), together with topographic effects, contributed to the development of the well-
27 documented Western Iberian Buoyant Plume (Peliz et al., 2002; Otero et al., 2008), which
28 strongly influenced the shelf circulation, forming an averaged veering to ~270° (measured
29 clockwise from the North) during 20th-21st of March, as reflected by in situ observations and
30 IBI outputs (Figure 6, c). However, GLOBAL could only partially reproduce the prevailing
31 surface flow as modelled currents were mainly advected to the south-southwest (180°-270°).
32 Equally, IBI appeared to correctly replicate the acceleration of the upper-layer stream from 10
33 to 45 cm·s⁻¹ due to impulsive-type freshwater river outflow already observed in situ estimations
34 of sea surface currents (Figure 6, d). Notwithstanding, GLOBAL current intensity remained
35 moderated (below 20 cm·s⁻¹) during most part of March, including the selected episode, as
36 reflected by the poorer skill metrics obtained. The current speed underestimation observed in
37 this tidal environment is mainly attributable to the fact that GLOBAL system provides a detided
38 solution, so barotropic tidal velocities do not contribute to the final prescribed total velocity.

39 Daily-averaged maps of modelled SSS and SST were computed for the 21st of March (Figure
40 6, e-h) to infer the differences between GLOBAL and IBI. As it can be seen, the former showed
41 a relatively-smoothed and spatially-homogeneous decrease in the salinity and temperature
42 fields along the entire coastline (Figure 6, e-f), while the latter exhibited more intricate patterns
43 with many filaments together with a significant drop in SSS and SST (Figure 6, g-h) in the
44 periphery of the three main local rivers mouth (from North to South: Miño, Douro and Tagus)
45 as a result of freshwater plumes flowing out over saltier Atlantic waters. In this three cases, the
46 SST field could effectively act as a tracer for the salinity stratification.

1 There is a significant resemblance between the monthly current roses derived from in situ
2 observations and IBI predictions in terms of speed and mean direction (Figure 6, i), showing
3 the predominance of the so-called Iberian Poleward Current, flowing northwards and circuiting
4 the western and northern Iberian margins under prevailing southerly winds (Torres and Barton,
5 2006). GLOBAL current outputs differed from observations, exhibiting an overall tendency for
6 eastward directions. The skill metrics derived from time series comparison at B4 buoy location
7 confirmed that the regional OOFS outperformed the global one during March 2018, hence
8 postulating the benefits of improved horizontal resolution to better resolve the plume dynamics
9 and its extension off-shelf. In addition, the increased horizontal resolution of IBI allows to better
10 resolving individual frontal fluctuations and horizontal salinity gradients by preserving the
11 signal of river plume narrower, closer to the coast and with a more complex structure. The
12 impact of model resolution in both the horizontal extent of the plume and the strength and
13 position of the freshwater front has been subject of previous studies (Bricheno et al., 2014).
14 Since both models present 50 depth levels and similar vertical discretization, the horizontal
15 resolution and the riverine forcing are assumed to play a primary role when attempting to
16 explain the differences encountered in models performance for this specific test-case.
17

18 **6 Circulation in the Strait of Gibraltar: multi-model inter-comparison from global to 19 coastal scales**

20 Proved the relevance of the intensity and orientation of the AJ in determining the surface
21 circulation of the Alboran Sea, the ability of each OOFS to portray the upper layer circulation
22 in the GIBST area has been evaluated. The annually-averaged surface pattern provided by the
23 HFR network revealed north-eastward speeds around $100 \text{ cm}\cdot\text{s}^{-1}$ in the narrowest section of the
24 Strait (Figure 7, a). SAMPA coastal model seemed to capture well the time-averaged intensity
25 and orientation of the Atlantic inflow (Figure 7, b), whereas IBI regional model clearly
26 overestimated the mean surface circulation speed (Figure 7, c). Finally, the coarser OOFS
27 (GLOBAL) barely captured the most basic features on the incoming flow and its subsequent
28 propagation towards the north-east (Figure 7, d).

29 As this qualitative model-intercomparison on a yearly basis was insufficient to infer the
30 skilfulness of each system, a quantitative validation at the midpoint of the selected transect
31 (white square in Figure 1-c) was assessed. The scatter plot of HFR-derived hourly current speed
32 versus direction (taking as reference the North and positive angles clockwise) revealed
33 interesting details (Figure 8, a): firstly, the AJ flowed predominantly eastwards, forming an
34 angle of 78° respect the North. The current velocity, on average, was $100 \text{ cm}\cdot\text{s}^{-1}$ and reached
35 peaks of $250 \text{ cm}\cdot\text{s}^{-1}$. Speeds below $50 \text{ cm}\cdot\text{s}^{-1}$ were registered along the entire range of
36 directions. Westwards currents, albeit minority, were also observed and tended to
37 predominantly form an angle of 270° .

38 The scatter plot of SAMPA estimations presented a significant resemblance in terms of
39 prevailing current velocity and direction (Figure 8, b). Although the time-averaged speed and
40 angle were slightly smaller ($90 \text{ cm}\cdot\text{s}^{-1}$) and greater (88°), respectively, the main features of the
41 AJ were qualitatively reproduced: maximum velocities (up to $250 \text{ cm}\cdot\text{s}^{-1}$) were associated with
42 an eastward flow and an AJ orientation in the range of 50° - 80° . Besides, surface flow reversals
43 to the west were properly captured.

44 By contrast, noticeable differences emerged in the scatter plot of regional IBI estimations
45 (Figure 8, c): surface current velocities below $30 \text{ cm}\cdot\text{s}^{-1}$ were barely replicated and the AJ
46 inversion was only observed very occasionally. Despite the fact that IBI appeared to properly
47 portray the mean characteristics of the eastwards flow, the model tended to privilege flow

1 directions comprised between 60° and 180° and to overestimate the current velocity, with
2 averaged and maximum speeds around 117 cm·s⁻¹ and 280 cm·s⁻¹, respectively.

3 In the case of the scatter plot derived from GLOBAL estimations, even more substantial
4 discrepancies were detected as the variability of both the AJ direction and speed were clearly
5 limited to the range 65°-80° and 50-200 cm·s⁻¹, respectively (Figure 8, d). No flow reversals
6 were detected and peak velocities of the eastward flow were underestimated.

7 The scatter plots of observation-model differences provided relevant information (Figure 8,
8 e-g). In the case of SAMPA, discrepancies were clustered around zero for both parameters, with
9 an asymptotic distribution along the main axes (Figure 8, e). On the contrary, a negative bias to
10 negative differences as observed for both IBI (Figure 8, f) and GLOBAL (Figure 8, g),
11 especially for the latter. In other words, the regional and global OOFSSs overestimated both the
12 current speed and the angle of the AJ, reflecting a tendency to more south-easterly directions
13 (clockwise rotated respect the north). Overall, a steady improvement in the AJ characterization
14 is evidenced in model performance when zooming from global to coastal configurations,
15 highlighting the benefits of the dynamical downscaling approach along with other relevant
16 factors such as a more detailed bathymetry, a higher spatio-temporal resolution of the
17 atmospheric forcing or the inclusion of accurate tidal and meteorologically-driven barotropic
18 velocities prescribed across the open boundaries. These results highlight the relevance of the
19 remote forcing in the flow reversals and how sub-tidal barotropic lateral forcing imposed in
20 SAMPA, obtained from NIVMAR storm surge model, ensures that SAMPA model captures a
21 realistic variability of inflow and outflow currents though the Strait. Therefore, the remote
22 barotropic effect of the meteorological forcing over the entire Mediterranean basin, which is
23 not included in IBI and GLOBAL systems, play a major role not only in the regulation of the
24 seasonal cycle of the AJ but also in the occasional inflow inversions, in accordance with
25 previous works (Macias et al., 2016).

26 Additional statistical indicators were computed: two histograms illustrated the number of
27 hourly zonal (U) and meridional (V) velocity data per class interval (Figure 9, a-b). HFR-
28 derived zonal velocity estimations exhibited a Gaussian-like shape clustered around 84 cm·s⁻¹
29 and slightly shifted to lower values in the case of SAMPA coastal model (79 cm·s⁻¹). Both
30 datasets show similar positive skew and variability, with the standard deviation around 56-57
31 cm·s⁻¹ for 2017 (Figure 9, a). IBI and GLOBAL presented narrowed histograms, with
32 distributions positively shifted and constrained to zonal velocities above 0 and 40 cm·s⁻¹,
33 respectively. In the case of meridional currents, each distribution exhibits a nearly symmetrical
34 Gaussian-like shape but shifted towards different values (Figure 9, b). Whilst SAMPA and IBI
35 exhibited an alike distribution (and moderately similar to that revealed for HFR estimations),
36 GLOBAL histogram emerged again dramatically shortened and restricted only to positive
37 values, revealing a recurrent predominance of the AJ to flow north-eastwards.

38 Based on the QQ-plot for the zonal velocity component (Figure 9, c), it can be concluded
39 that SAMPA estimations were consistent despite the slight overestimation observed for the
40 highest velocities (95th-100th percentiles). The general IBI overestimation along the entire range
41 of percentiles was also clearly evidenced. In accordance with its histogram, GLOBAL system
42 overestimated (underestimated) zonal currents below (above) the 90th percentile. A similar
43 behaviour was also observed for GLOBAL meridional velocities, this time around the 20th
44 percentile (Figure 9, d). On the contrary, both SAMPA and IBI appeared to generally
45 underestimate the meridional surface current speed, even more for higher percentiles.

46 Class-2 skill metrics, gathered in Table 3, were also computed in order to provide a
47 quantitative perspective of models performance at the midpoint of the selected transect (white

square in Figure 1-c). SAMPA clearly outperformed both systems, as reflected by lower RMSD values for both velocity components together with a complex correlation coefficient (CCC) and phase (CCP) of 0.79 and -8°, respectively, which means that SAMPA predictions were highly correlated with HFR current observations although slightly clockwise rotated (i.e., more south-eastwards). The agreement between HFR hourly data and IBI and GLOBAL estimations, albeit significant (CCC above 0.6), was lower as the related phase values decreased substantially (especially for GLOBAL: CCP below -20°), indicating a more zonal surface flow.

The three systems predicted more precisely the zonal velocity component than the meridional one, with scalar correlations emerging in the ranges [0.68-0.83] and [0.15-0.56], respectively. Notwithstanding, RMSD were more moderate for the latter (below 37 cm·s⁻¹) than for the former (below 53 cm·s⁻¹). This could be attributed to the extremely intense and predominant West-East zonal exchange of Atlantic-Mediterranean waters through GIBST, with the meridional flow playing a residual role.

The statistical results derived from SAMPA-HFR comparison, gathered in Table 3, are in line with those earlier obtained in a 20-month validation performed by Soto-Navarro et al. (2016), which reported correlations of 0.70 and 0.27 for the zonal and meridional velocities, respectively. The observed model-radar discrepancies might be attributed to the fact that the uppermost z-level of SAMPA model is 2.5 m, while HFR observations are representative of the first 0.5 m of the water column and thus more sensitive to wind forcing. This might explain some model drawbacks detected in relation to the reduced energy content in surface current speeds, as reflected by the positive bias between HFR estimations and SAMPA outputs (Table 3)

Complementarily, the multi-model inter-comparison exercise in the GIBST region focused on the ability to adequately reproduce an extreme event: the quasi-permanent full reversal of the AJ surface flow during, at least, 48 hours when intense easterlies episodes were prevalent. Under this premise, only four episodes were detected and categorized during the entire 2017 (Figure 10). The prevailing synoptic conditions were inferred from ECMWF predictions of sea level pressure (SLP: Figure 10, a-d) and zonal wind at 10 m height (U-10: Figure 10, e-h). A significant latitudinal gradient of SLP was observed in 3 episodes (February, March and December), with high pressures over the Gulf of Biscay and isobars closely spaced in GIBST, giving rise to very strong easterlies (above 10 m·s⁻¹), channelled through the Strait (Figure 10: e, f and h). In August, the typical summer weather type was observed with Azores High pressures governing the Atlantic Area and moderate but persistent easterly winds blowing through the entire Western Mediterranean (Figure 10: c, g).

Both atmospheric variables were spatially-averaged over specific sub-regions (WSMED and GIBST, respectively, indicated by a red square in Figure 10: a-h) and 3-hourly monitored along the selected months (Figure 10: i-p). Very high SLP values and extremely high (negative) U-10 (i.e., intense easterlies) led to a complete inversion of the surface flow, from the prevailing eastward direction to a westward outflow into the Atlantic Ocean, as reflected in the Hovmöller diagrams computed for the HFR-derived zonal currents (Figure 10, q-t). In February, a brief 24-h inversion (related to less intense easterlies) preceded the full reversal of the surface flow (Figure 10, q). Likewise, the event detected in March consisted of an abrupt interruption and complete reversal of the eastwards AJ (Figure 10, r). By contrast, in August and December, the classical AJ intense inflow (above 100 cm·s⁻¹) into the Mediterranean was only observed in the southern part of the transect, whereas in the northern sector some fluctuations between weaker eastward and westward currents were evidenced, mainly associated with changes in the prevalent wind regime (Figure 10, s-t). Under persistent easterlies, a weaker coastal counter

1 current was detected flowing westwards and bordering the Spanish shoreline (Figure 10, s).
2 Such coastal flow inversion has been previously reported and subject to further analysis by
3 Reyes et al. (2015). Particularly, the flow reversal detected in August was not triggered by high
4 SLP (Figure 10, k) but induced by moderate and persistent easterlies ($5 \text{ m}\cdot\text{s}^{-1}$, Figure 10-o).

5 Short-lived reversals of the surface inflow have been previously reported to occur almost
6 every tidal cycle in Camarinal Sill (western end of GIBST: Figure 1-b) mainly due to the
7 contribution of the semidiurnal tidal component M_2 (Reyes, 2015; Sannino, et al. 2004; García
8 Lafuente, et al., 1990; La Violette and Lacombe 1988). Since the mean inflow of Atlantic water
9 is modulated by barotropic tidal currents, hourly-averaged sea surface height (SSH)
10 observations provided by Tarifa tide-gauge (Figure 1, c) were used to elucidate if the four 2-
11 day inflow reversal events in the eastern end of the Strait could have been mostly influenced by
12 spring-neap tidal cycle fluctuations (Figure 10, u-x). Although the fortnightly variability was
13 clearly observable in a monthly time series of SSH, no cause-effect relationship could be
14 visually inferred from the inspection of zonal velocities at the selected transect (Figure 10, q-
15 t). Apparently, evidence of preference for a specific tidal cycle was not observed as the four
16 flow reversal episodes took place under strong easterlies but during different tidal conditions,
17 ranging from neap tides (Figure 10, u) to spring tides (Figure 10: v, x). As shown in Lorente et
18 al. (2018), tides seemed to play a secondary role by partially speeding up or slowing down the
19 westward currents, depending on the phase of the tide. These results are in accordance with
20 previous modelling studies (Sannino et al., 2004) where the contribution of the semidiurnal tidal
21 component to the transport was proved to be relevant over the Camarinal Sill, (incrementing
22 the mean transport by about 30%, for both the inflow and the outflow), whereas it was almost
23 negligible at the eastern end of the Strait.

24 The observed 2-day averaged HFR-derived circulation patterns associated with the four
25 events here studied were depicted in Figure 11 (a, e, i, m). Some common peculiarities were
26 exposed, such as the overall westward outflow through the narrowest section of GIBST or the
27 subtle anticyclonic inflow into the Algeciras Bay. Three study cases revealed a predominant
28 circulation towards the West together with a marked acceleration of the flow in the periphery
29 of Algeciras Bay, reaching speeds above $70 \text{ cm}\cdot\text{s}^{-1}$ (Figure 11: a, e, i). The fourth case
30 (December 2017) was substantially less energetic and exhibited a rather counter-clockwise
31 recirculation in the entrance to GIBST. (Figure 11, m). On the other hand, two episodes
32 illustrated how the circulation in the easternmost region of the study domain followed a
33 clockwise rotation (Figure 11: e, m).

34 From a qualitative perspective, SAMPA was able to reproduce fairly well at least two of the
35 four inversion episodes in terms of overall circulation pattern in GIBST and adjacent waters
36 (Figure 11: f, j, n). In the event of March, SAMPA replicated the intense eastern anticyclonic
37 gyre, with velocities up to $80 \text{ cm}\cdot\text{s}^{-1}$, along with the inflow into the Algeciras Bay. However,
38 the model could only partially resolve the AJ inversion, exhibiting a counter-clockwise
39 recirculation with the outflow restricted to the north-western Spanish shoreline (Figure 11, f).
40 In the episode corresponding to 4th–5th of December (Figure 11, n), the upper-layer dynamic
41 was rather similar to the previously described for March, albeit less vigorous. The visual
42 resemblance with HFR map (Figure 11, m) was generally high, according to common features
43 observed: the eastern anticyclonic gyre, the central belt of currents circulating towards the
44 North-West and eventually the cyclonic recirculation structure in the entrance to GIBST. On
45 the contrary, in the event occurred between 14th-15th of August (Figure 11, j), a moderate
46 observation-model resemblance was deduced in the northeastern sector of the domain: SAMPA
47 was able to resolve the observed southwestward stream, the inflow into the Algeciras Bay and
48 the weak intrusion of Mediterranean waters into GIBST bordering the northern shoreline but,

1 by contrast, it was ultimately impelled to join the general AJ inflow governing the Strait and
2 propagating towards the east. Finally, although SAMPA predicted the occurrence AJ reversal
3 by 20th–21st of February (Figure 11, b), the simulated circulation structure partially differed
4 from that observed with HFR estimations (Figure 11, a). Whereas the formed prognosticated a
5 meander-like circulation, a predominant cross-shore stream within the channel and a flow
6 inversion uniquely circumscribed to the entrance of GIBST, the latter provided an overall
7 westward outflow from the Mediterranean Sea into the Atlantic Ocean.

8 In the case of IBI, the Atlantic inflow was always present. In two episodes, the intense AJ
9 was directed towards the North-East (Figure 11: g, o), converging with the overall clock-wise
10 gyre that dominated the easternmost region, which was already observed in HFR estimations
11 (Figure 11: e, m). By contrast, in the two remaining episodes the surface inflow was
12 predominantly zonal (Figure 11, c) and directed south-eastwards (Figure 11, k), respectively.
13 Whereas in the former event no common features could be observed between the HFR and IBI,
14 in the latter a moderate observation-model resemblance was deduced in the northeastern sector
15 of the domain, as similarly occurred with SAMPA estimations (Figure 11, j). Leaving aside the
16 counter-clockwise eddy observed in IBI pattern (Figure 11, k), absent from HFR map (Figure
17 11, i), IBI partially resolved the observed southwestward flow, the circulation into the Algeciras
18 Bay and the westward penetration of surface waters along the northern shoreline of the Strait.
19 Finally, GLOBAL system barely replicated the HFR-derived circulation patterns as the
20 northeastward stream was permanently locked, showing further reduced speed variations from
21 one episode to another (Figure 11: d, h, l, p).

22 The reversal of the surface inflow is caused by meteorological-driven flows through the
23 Strait associated with the passage of high pressure areas over the Mediterranean (García-
24 Lafuente et al. 2002). Because these flows originate in the far field and not in the Strait itself,
25 the different grid resolution of IBI and SAMPA do not appear the likely explanation for these
26 events to do not show up in the IBI model. Instead, their different skill in capturing such extreme
27 events seems to be associated to their different forcing.

28 Among the physical implications of the surface inflow reversal, abrupt increases in the SST
29 field were revealed, especially during summertime when warmer surface waters outflowed into
30 the Atlantic from the Mediterranean (Figure 12). During August 2017, the aforementioned CCC
31 raised the day 11th and lasted until the end of the month, confined at higher latitudes except for
32 the already analysed 2-day event of 14th-15th, coinciding with the full reversal mentioned
33 (Figure 12, a). The monthly inter-comparison of the zonal currents at the midpoint of the
34 selected transect (represented by a black square in Figure 12-a) confirmed the progressive
35 improvement in the skill metrics obtained (Figure 12-b, right box) thanks to both the multi-
36 nesting strategy and the inclusion of accurate tidal forcing. SAMPA and IBI were able to
37 accurately reproduce the wide tidal oscillations, although only the former could properly
38 capture the flow inversions represented by negative zonal velocities that took place between the
39 14th-15th and between 21st-24th of August (Figure 12, b), as SAMPA properly resolves the
40 meteorologically-driven (barotropic) currents through the Strait, imported from NIVMAR
41 storm surge model. GLOBAL detided outputs only reproduced basic features of the surface
42 flow, showing always smoothed eastward velocities. As a consequence, skill metrics for the
43 coastal OOFS were better than for the regional system, and recursively skill metrics for IBI
44 were in turn better than global ones, in terms of higher (lower) correlation (RMSD) values.
45 Analysis for the meridional velocity component (not shown) revealed similar results, with the
46 SAMPA outperforming the coarser models. Notwithstanding, the three OOFS proved to be
47 more skilled to forecast zonal than meridional currents. The complex correlation coefficient
48 and the related phase were 0.85 and -7.37° , (Figure 12-b, black box in the right side)

1 respectively, indicating both the relevant SAMPA-HFR agreement and the slight veering of
2 model outputs respect HFR estimations: a negative value denoted a clockwise rotation of
3 modelled current vectors (i.e., a more southwardly direction). In the case of IBI, although the
4 phase was similar (-7.92°) the complex correlation was lower (0.72). GLOBAL current vectors
5 were, on average, significantly veered clockwise (-25.71°), despite the high complex correlation
6 coefficient (0.70).

7 From the 11th to the 17th of August, a progressive warming of 7.5°C at the upper ocean layer
8 of the northern shoreline was observed (Figure 12, c), according to the in situ estimations
9 provided by B7 buoy (whose latitude is located with a solid black dot in Figure 12-a). As
10 easterly winds progressively dominated the study-area and persisted enough, the CCC
11 broadened and the complete inflow reversal transported warmer Mediterranean waters to the
12 west through the entire transect, as reflected by the pronounced SST maximum (~25°C)
13 detected soon afterwards, by the 18th of August. A secondary peak of SST was monitored by
14 the 25th, before the CCC started weakening. In accordance with previous statements about
15 model behaviour for the zonal currents, once again SAMPA outperformed the coarser systems
16 as reflected by a significantly high correlation of 0.89 and a lower but statistically relevant
17 RMSD of 1.22°C. IBI presented a general bias (positive the first week of august and negative
18 the rest of the month) but adequately reproduced the temporal variability of the SST field
19 (correlation of 0.67). In the case of GLOBAL, the system could not benefit from data
20 assimilation in this intricate coastal area with low level of available observations: worse skill
21 metrics were subsequently obtained, with a correlation of 0.65 and a RMSD above 2°C.

22 Finally, outputs from SAMPA high-resolution coastal model were used to provide further
23 insight into the entire AJ-WAG system and how diversity from the classical picture of the
24 Alboran Sea surface circulation emerged from changes in the intensity and direction of the AJ.
25 Although only one episode (corresponding to December 2017) is here shown (Figure 13), the
26 four events followed a similar scenario:

- 27 i) *Prelude*: the AJ was observed flowing vigorously (with velocities clearly above 80 cm·s⁻¹)
28 into the Alboran Sea with a rather zonal direction (Figure 13-a), heading northeast later on,
29 surrounding and feeding the WAG, which appeared to be slightly detached from its
30 traditional position in the Western Alboran Sea (Figure 13, b).
- 31 ii) *Onset*: as westerly wind lost strength, the AJ speed became progressively weaker and tended
32 to flow more southwardly, giving rise to a weakening and subsequent decoupling of the AJ-
33 WAG system along with the reinforcement of an already existing small-scale coastal eddy
34 that coexisted with the WAG (Figure 13, c-d). Circulation snapshots with three gyres
35 (including the EAG, out of the pictures) have been previously reported in the literature
36 (Flexas et al., 2006; Viúdez et al., 1998). This coastal eddy could be either cyclonic and
37 confined northeast of Algeciras Bay (February 2017, not shown) or be anticyclonic, starting
38 to grow, detach from the coast and migrate eastwards as a result of both the change in AJ
39 orientation and the WAG displacement (Figure 13, e-f). Meanwhile, the WAG presented
40 different configurations: from an almost-symmetric aspect (August 2017, not shown) to a
41 more elongated shape in the cross-shore direction (December 2017: Figure 13-f) or in the
42 along-shore direction (March 2017, not shown).
- 43 iii) *Development*: The AJ velocity reached a minimum (below 50 cm·s⁻¹) associated with a sharp
44 change in the predominant wind regime from westerlies to easterlies (Figure 13, g-h). A
45 branch of the eddy, neighboring the Strait, was wind-weakened and deflected from the main
46 rotating pathway and started to flow westwards to the GIBST.

1 iv) *Full establishment of the inflow reversal*: complete westward outflow from the
2 Mediterranean Sea into the Atlantic Ocean through the narrowest section of GIBST, reaching
3 a peak of velocity over Camarinal Sill (Figure 13, i). The migratory eddy and the WAG
4 started merging into one single anticyclonic gyre (Figure 13, j).

5 v) *Epilogue*: Afterwards, in three of the cases the re-settlement of predominant westerlies
6 (Figure 10: m, n, p) favoured the return of the northeastward oriented Atlantic inflow and
7 the consequent reactivation of the usual AJ-WAG system (not shown). By contrast, in the
8 fourth episode (August 2017), summer easterly winds kept blowing moderately for two extra
9 weeks (Figure 10, o) but were too weak to preserve the induced reversal, thus the Atlantic
10 inflow reappeared again.

11 12 7 Conclusions

13 The current generation of ocean models have undergone meticulous tuning based on several
14 decades of experience. The ever-increasing inventory of operational ocean forecasting systems
15 provides the society with a significant wealth of valuable information for high-stakes decision-
16 making and coastal management. Some of them are routinely operated on overlapping regions,
17 offering the opportunity to compare them, judge the strengths and weaknesses of each system
18 and eventually evaluate the added-value of high-resolution coastal models respect to coarser
19 model solutions.

20 In this work, a multi-parameter model inter-comparison was conducted at the sea surface,
21 ranging from global to local scales in a two-phase stepwise strategy. Firstly, a comparison of
22 CMEMS products (GLOBAL and the nested IBI regional system) was performed against
23 remote-sensed and in situ observations. In terms of temperature, results highlighted the overall
24 benefits of both the GLOBAL direct data assimilation in open-waters and the increased
25 horizontal resolution of IBI in coastal areas, respectively. GLOBAL seemed to replicate slightly
26 better the SST field likely thanks to recent progresses in data assimilation schemes and to the
27 growing wealth of available observational data. In this context, the assimilation of new types
28 of observations (drifting buoys SST) should improve constrains in modeled variables and
29 overcome the deficiencies of the background errors, in particular for extrapolated and/or poorly
30 observed variables (Gasparin et al., 2018; Lellouche et al., 2018). In the open sea, IBI benefited
31 indirectly from the data assimilation conducted in its parent system thanks to the spectral
32 nudging technique, allowing thereby the regional and global model states to be reconciled with
33 each other. IBI even outperformed GLOBAL locally in specific open-water zones such as the
34 continental shelf break. IBI performance was also more accurate in those coastal regions
35 characterized by a jagged coastline and a substantial slope bathymetry. As GLOBAL has a
36 smoothed bathymetry and do not resolve many narrow features of the real sea floor, the depths
37 where mixing takes place could be biased. Besides, those mixing processes acting at scales
38 smaller than the grid cell size might substantially affect the resolved large-scale flow in the
39 coarser GLOBAL system.

40 On the other hand, since GLOBAL is a detided model solution, tidally-driven mixing could
41 account for a portion of the discrepancies found between GLOBAL and satellite-derived SST
42 estimations in energetic tidal areas such as the English Channel, the North Sea and the Irish
43 Sea. Whereas GLOBAL seemed to predict an over-stratification in shelf-seas, IBI could better
44 reproduce the vertical stratification and hence the SST field in the aforementioned subregions.

45 Complementarily, an isolated but rather illustrative example of the impact of impulsive-type
46 river freshwater discharge on local surface circulation in NW Spain was provided. The

1 increased horizontal resolution of IBI allowed a more accurate representation of horizontal
2 salinity gradients, the horizontal extent of the plume and the strength and position of the
3 freshwater front, according to the results derived from the validation against in situ observations
4 of SSS, SST and currents provided by a moored buoy. Since both GLOBAL and IBI present 50
5 depth levels, similar vertical discretization and comparable climatological runoff forcing, the
6 horizontal resolution is assumed to play a primary role when attempting to explain the
7 differences encountered in models performance for this specific test-case. Notwithstanding, the
8 authors are fully aware of this single isolated example does not suffice and additional events
9 over the entire IBI coastal domain should be examined in future works.

10 Finally, a 1-year (2017) multi-model inter-comparison exercise was performed in the Strait
11 of Gibraltar between GLOBAL, IBI and SAMPA coastal system in order to elucidate the
12 accuracy of each OOFS to characterize the AJ dynamic. A quantitative comparison against
13 hourly HFR estimations highlighted both the steady improvement in AJ representation when
14 moving from global to coastal scales though a multi-nesting model approach and also the
15 relevance of a variety of factors at local scales, among others:

- 16 i) A sufficiently detailed representation of bathymetric features: the very high horizontal
17 resolution of SAMPA (~ 400 m) and, consequently, the tailored bathymetry employed in
18 order to capture small-scale ocean process and resolve sharp topographic details.
- 19 ii) A better representation of air-sea interactions: the adequate refinement of the spatio-
20 temporal resolution of the atmospheric forcing used in SAMPA, especially in a complex
21 coastal region where topographical steering further impacts on flows.
- 22 iii) The nesting strategy implemented in SAMPA, where the coastal model is forced not only
23 by daily fields provided by the regional IBI system but also by outputs from Mog2D and
24 NIVMAR models. The additional inclusion of these accurate tidal and meteorologically-
25 driven barotropic velocities, respectively, allowed a detailed characterization of the
26 variability of the surface Atlantic inflow, including persistent full reversal episodes.
27 Although the matching between HFR observations and SAMPA outputs is mainly found
28 in two of the four reversal events detected, this result demonstrates its added value as
29 modelling tool towards the comprehension of such singular oceanographic event. A
30 detailed characterization of this phenomenon is relevant from diverse aspects,
31 encompassing search and rescue operations, the management of accidental marine
32 pollution episodes, or safe ship routing.

33 Finally, SAMPA coastal model outputs were analysed in order to put in a broader
34 perspective the context of the onset, development and end of such flow reversal and its impact
35 on the AJ-WAG coupled system. The synergistic approach based on the integration of HFR
36 observing network and SAMPA predictive model has proved to be valid to comprehensively
37 characterize the highly dynamic coastal circulation in the GIBST and the aforementioned
38 episodic full reversals of the surface inflow. In this context, data assimilation (DA) would
39 provide the integrative framework for maximizing the joint utility of HFR-derived observations
40 and coastal circulation models. A DA scheme could be incorporated in future operational
41 versions of SAMPA in order to improve its predictive skills, since similar initiatives are
42 currently ongoing with positive results (Vandenbulcke et al., 2017; Stanev et al., 2015).
43 Although DA is a powerful technique, advances in coastal ocean modelling should also
44 encompass an improved understanding of high frequency small-scale physical processes, the
45 accurate model parameterization of the effects triggered by such sub-grid phenomena and the
46 integration of air-sea, wave-current and biophysical interactions by means of coupled
47 forecasting systems (Wilkin et al., 2017). Complementarily, as part of possible next

1 improvements of SAMPA system, we will explore the possibility of a more direct nesting
2 strategy into IBI since the current operational version of IBI includes the delivery of 3D hourly
3 outputs.

4 Future efforts are planned to improve CMEMS global and regional OOFSS in several aspects
5 already addressed in the present work. While GLOBAL system will be evolved towards a $1/36^{\circ}$
6 model application, a substantial refinement will be accomplished for regional IBI system in
7 both vertical and horizontal resolutions: from 50 to 75 depth layers and from $1/36^{\circ}$ to $1/108^{\circ}$
8 (~ 1 km), respectively. Whereas the first feature will be incorporated during CMEMS Phase-2
9 (2018-2021), the second milestone will be achieved in the frame of Inmerse H2020 project and
10 is expected to positively impact on a more accurate representation of coastal processes, among
11 others: submesoscale shelf break exchanges and connectivity, fronts, river plumes or
12 topographic controls on circulation. In addition, a more detailed bathymetry is expected to be
13 introduced in future operational versions of IBI in order to better resolve those regions with
14 complex coastline and intricate bottom topography. Other factors that could be potentially
15 improved but still deserve further analysis are the air-sea and the land-sea interactions, i.e., the
16 meteorological and riverine forcings. With regards to the former, a more skilful atmospheric
17 forecast model with a higher spatiotemporal resolution (i.e., hourly prediction over a more
18 refined grid) could aid to better represent the coastal circulation by a more accurate
19 discrimination of the topographic structures and the replication of the inertial oscillations and
20 mesoscale processes. On the other hand, each main river basin hydrology should be more
21 accurately represented with daily-updated outputs from tailored hydrological models. Finally,
22 refined mixing schemes might also produce notable improvement in the representation of water
23 masses, resulting in a substantial reduction of temperature and salinity bias relative to model
24 solution.

25

26

27

28

29

30

31

32

33

34

35

36

37

38

39

40

41

1 **References**

2 Álvarez-Fanjul, E., Pérez, B. and Rodríguez, B.: A description of the tides in the Eastern North
3 Atlantic, *Progress in Oceanography*, 40, 217–244, 1997.

4 Álvarez-Fanjul., E., Pérez, B. and Rodríguez, I.: Nivmar: a storm surge forecasting system for
5 Spanish waters, *Sci. Mar.*, 65, 145-154, 2001.

6 Álvarez-Fanjul et al.: Operational Oceanography at the Service of the Ports. In “New Frontiers
7 in Operational Oceanography”. E. Chassignet, A. Pascual, J. Tintoré and J. Verron, Eds.,
8 GODAE OceanView, 729-736, doi:10.17125/gov2018.ch27, 2018.

9 Aznar, R., Sotillo, M.G., Cailleau, S., Lorente P., Levier, B., Amo-Baladrón, A., Reffray, G.
10 and Álvarez-Fanjul, E.: Strengths and weaknesses of the Copernicus forecasted and
11 reanalyzed solutions for the Iberia-Biscay-Ireland (IBI) waters, *Journal of Marine Systems*,
12 159, 1-14, 2016.

13 Brasseur, P., Bahurel, P., Bertino, L., Birol, F., Brankart, J.M., Ferry, N., Losa, S., Remy, E.,
14 Schröter, J., Skachko, S., Testut, C.-E., Tranchant, B., Van Leeuwen, P.J. and Verron, J.:
15 Data assimilation for marine monitoring and prediction: the MERCATOR operational
16 assimilation systems and the MERSEA developments, *Q. J. R. Meteorol. Soc.*, 131, 3561-
17 3582, doi: 10.1256/qj.05.142, 2005.

18 Bricheno, L.M, Wolf, J.M. and Brown, J.M.: Impacts of high resolution model downscaling in
19 coastal regions, *Continental Shelf Research*, 87, 7-16, 2014.

20 Caldeira, R., Couvelard, X., Vieira, R., Lucas, C., Sala, I. and Vallés Casanova, I.: Challenges
21 on building an operational forecasting system for small island regions: regional to local,
22 *Journal of Operational Oceanography*, 9, 1-12, 2016.

23 Carrere, L. and Lyard, F.: Modelling the barotropic response of the global ocean to atmospheric
24 wind and pressure forcing – comparisons with observations, *Geophys. Res. Lett.*, 30 (6),
25 1-8, 2003.

26 Cats, G. and Wolters, L.: The Hirlam project, *International Journal of Computational Science
27 and Engineering*, 3, 4-7, 1996.

28 Chioua, J., Dastis, C., Gonzalez, C.J., Reyes, E., Mañanes, R., Ruiz, M.I., Álvarez-Fanjul, E.,
29 Yanguas, F., Romero, J., Álvarez, O. and Bruno, M.: Water exchange between Algeciras
30 Bay and the Strait of Gibraltar: a study based on HF coastal radar, *Estuarine Coastal and
31 Shelf science*, 196, 109-122. doi: 10.1016/j.ecss.2017.06.030, 2017.

32 Cotelo, C., Amo-Baladrón, A., Aznar, R, Lorente, P., Rey, P. and Rodriguez, A.: On the
33 successful coexistence of oceanographic operational services with other computational
34 workloads, *International Journal of High Performance Computing Applications*, 1-12, doi:
35 10.1177/1094342017692045, 2017.

36 Cucco, A., Sinerchia, M., Ribotti, A., Olita, A., Fazioli, L., Perilli, A., Sorgente, B., Borghini,
37 M., Schroeder, K. and Sorgente, R.: A high-resolution real-time forecasting system for
38 predicting the fate of oil spills in the Strait of Bonifacio (western Mediterranean Sea). *Marine
39 Pollution Bulletin*, 64 (6), 1186–1200, 2012.

40 Dai, A., Qian, T., Trenberth, K. and Milliman, J.D.: Changes in continental freshwater
41 discharge from 1948 to 2004, *J. Climate*, 22, 2773-2792, 2009.

42 Dastis, C., Izquierdo, A., Bruno, M., Reyes, E., Sofina, E.V. and Plink, N.L.: Influence of the
43 atmospheric pressure fluctuations over the Mediterranean Sea on the mesoscale water

1 dynamics of the Strait of Gibraltar and the Alboran Sea, Fundamentalnaya i Prikladnaya
2 Gidrofizika, 11 (1), 28-29, doi: 10.7868/S2073667318010033, 2018.

3 Dorman, C.E., Beardsley, R.C. and Limeburner, R.: Winds in the Strait of Gibraltar, Q.J.
4 Meteorol. Soc., 121, 1903-1921, 1995.

5 Egbert, G.D. and Erofeeva, S.Y.: Efficient inverse modeling of barotropic ocean tides, Journal
6 of Atmospheric and Oceanic Technology, 19, 183–204, 2002.

7 Federico, I., Pinardi, N., Coppini, G., Oddo, P., Lecci, R. and Mossa, M.: Coastal ocean
8 forecasting with an unstructured grid model in the southern Adriatic and northern Ionian
9 seas, Nat. Hazards Earth Syst. Sci., 17, 45-59, 2017.

10 Ferrarin, C., Roland, A., Bajo, M., Umgieser, G., Cucco, A., Davolio, S., Buzzi, A., Malguzzi,
11 P. and Drofa, O.: Tide-surge-wave modelling and forecasting in the Mediterranean Sea with
12 focus on the Italian coast. Ocean Modelling, 61, 38–48, 2013.

13 Ferrarin, C., Bellafiore, D., Sannino, G., Bajo, M. and Umgieser, G.: Tidal dynamics in the
14 inter-connected Mediterranean, Marmara, Black and Azov seas. Progress in Oceanography,
15 161, 102–115, 2018.

16 Ferrarin, C., Davolio, S., Bellafiore, D., Ghezzo, M., Maicu, F., Mc Kiver, W., Drofa, O.,
17 Umgieser, G., Bajo, M., De Pascalis, F., Malguzzi, P., Zaggia, L., Lorenzetti, G. and Manfè,
18 G.: Cross-scale operational oceanography in the Adriatic Sea. Journal of Operational
19 Oceanography, doi:10.1080/1755876X.2019.1576275, 2019.

20 Flexas, M., Gomis, D., Ruiz, S., Pascual, A. and Leon, P.: In situ and satellite observations of
21 the eastward migration of the Western Alboran Sea Gyre, Prog. Oceanogr., 70, 486-509,
22 2006.

23 García-Lafuente, J., Almazán, J.L., Fernández, F., Khribeche, A. and Hakimi, A.: Sea level in
24 the Strait of Gibraltar: Tides, Int. Hydrogr. Rev., LXVII, 111–130, 1990.

25 García-Lafuente, J., Delgado, J. and Criado, F.: Inflow interruption by meteorological forcing
26 in the Strait of Gibraltar, Geophysical Research Letters, 29 (19), 1914, 2002.

27 García-Lafuente, J., Álvarez-Fanjul, E., Vargas, J.M. and Ratsimandresy, A.W.: Subinertial
28 variability in the flow through the Strait of Gibraltar, J. Geophys. Res.: Oceans, 107 (C10),
29 3168, doi:10.1029/2001JC001104, 2002.

30 Gasparin, F., Greiner, E., Lellouche, J.M., Legalloudec, O., Garric, G., Drillet, Y., Bourdallé-
31 Badie, R., Le Traon, P.Y., Rémy, E. and Drévillon, M.: A large-scale view of oceanic
32 variability from 2007 to 2015 in the global high resolution monitoring and forecasting
33 system at Mercator Ocean, Journal of Marine Systems, 187, 260-276, doi:
34 10.1016/j.jmarsys.2018.06.015, 2018.

35 Graham, J. A., O'Dea, E., Holt, J., Polton, J., Hewitt, H. T., Furner, R., Guihou, K., Brereton,
36 A., Arnold, A., Wakelin, S., Castillo Sanchez, J. M., and Mayorga Adame, C. G.: AMM15:
37 a new high-resolution NEMO configuration for operational simulation of the European
38 North-West shelf, Geosci. Model Dev., 11, 681-696, 2018.

39 Greenberg, D.A., Dupont, F., Lyard, F.H., Lynch, D.R. and Werner, F.E.: Resolution issues in
40 numerical models of oceanic and coastal circulation, Continental Shelf Research 27, 1317-
41 1343, 2007.

1 Grifoll, M., Jordá, G., Sotillo, M.G., Ferrer, L., Espino, M., Sánchez-Arcilla, A. and Álvarez-
 2 Fanjul, E.: Water circulation forecasting in Spanish harbours. *Scientia Marina*, 76, S1, 45-
 3 61, doi: 10.3989/scimar.03606.18B, 2012.

4 Herbert, G., Garreau, P., Garnier, V., Dumas, F., Cailleau, S., Chanut, J., Levier, B., and Aznar,
 5 R.: Downscaling from oceanic global circulation model towards regional and coastal model
 6 using spectral nudging techniques: application to the Mediterranean Sea and IBI area
 7 models, *Mercator Ocean Quarterly Newsletters*, 49, 44, April 2014.

8 Hernández, F., Smith, G., Baetens, K., Cossarini, G., García-Hermosa, I., Drévillon, M.,
 9 Maksymczuk, J., Melet, A., Régner, C., Von Schuckmann, K.: Measuring performances,
 10 skill and accuracy in operational oceanography: New challenges and approaches. In “New
 11 Frontiers in Operational Oceanography”. E. Chassignet, A. Pascual, J. Tintoré and J. Verron,
 12 Eds., GODAE OceanView, 759-796, doi:10.17125/gov2018.ch29, 2018.

13 Hlevca, B., Wells, M.G., Cruz Font, L., Doka, S.E., Portiss, R., John, M.S. and Cooke, S.J.:
 14 Water circulation in Toronto Harbour, *Aquatic Ecosystems Health and Management*, doi:
 15 10.1080/14634988.2018.1500059, 2018.

16 Holt, J., Hyder, P., Ashworth, M., Harle, J., Hewitt, H.T., Liu, H., New, A.L., Pickles, S., Porter,
 17 A., Popova, E., Allen, J.I., Siddorn, J. and Wood, R.: Prospects for improving the
 18 representation of coastal and shelf seas in global ocean models, *Geosciences Model
 19 Development*, 10, 499-523, 2017.

20 Katavouta, A. and Thompson K.R. Downscalling ocean conditions with application to the Gulf
 21 of Maine, Scotian shelf and adjacent deep ocean, *Ocean Modelling*, 104, 54-72, 2016.

22 Kourafalou, V.H., De Mey, P., Staneva, J., Ayoub, N., Barth, A., Chao, Y., Cirano, M., Fiechter,
 23 J., Herzfeld, M., Kurapov, A., moore, A.M., Oddo, P., Pullen, J., Van der Westhuysen, A.
 24 and Weisberg, R.: Coastal Ocean Forecasting: science drivers and user benefits, *Journal of
 25 Operational Oceanography*, 8 (1), Special Issue: GODAE Oceanview part 1, 147-167,
 26 doi:10.1080/1755876X.2015.1022348, 2015.

27 Large, W.G. and Yeager, S.G.: Diurnal to decadal global forcing for ocean and sea-ice models:
 28 the data sets and flux climatologies, *NCAR technical notes*, 2004.

29 La Violette, P.E. and Lacombe, H.: Tidal-induced pulses in the flow through the Strait of
 30 Gibraltar, In *Oceanol. Acta*, Special Issue 0399-1784, *Océanographie Pélagique
 31 Méditerranéenne*, Villefranche-sur-Mer, France, Minas, H.J., Nival, P., Eds., 13–27, 1988.

32 Law Chune, S., Nouel, L., Fernández, E. and Derval, C. *PRODUCT USER MANUAL for the
 33 GLOBAL Ocean Sea Physical Analysis and Forecasting Products
 34 GLOBAL_ANALYSIS_FORECAST_PHY_001_024*, Copernicus Marine Environment
 35 Monitoring Service, April 2019.

36 Lellouche, J.-M., Greiner, E., Le Galloudec, O., Garric, G., Regnier, C., Drevillon, M.,
 37 Benkiran, M., Testut, C.E., Bourdalle-Badie, R., Gasparin, F., Hernández, O, Levier, B.,
 38 Drillet, Y., Remy, E. and Le Traon, P.Y.: Recent updates to the Copernicus marine Service
 39 global ocean monitoring and forecasting real-time 1/12° high resolution system, *Ocean
 40 Science*, 14, 1093-1126, 2018.

41 Lellouche, J.-M., Le Galloudec, O., Drévillon, M., Régner, C., Greiner, E., Garric, G.,
 42 Ferry, N., Desportes, C., Testut, C.-E., Bricaud, C., Bourdallé-Badie, R., Tranchant, B.,
 43 Benkiran, M., Drillet, Y., Daudin, A. and De Nicola, C.: Evaluation of global monitoring
 44 and forecasting systems at Mercator Océan, *Ocean Sci.*, 9, 57-81, 2013.

1 Le Traon, P.Y. et al.: The Copernicus Marine Environmental Monitoring Service: Main
2 Scientific Achievements and Future Prospects, *Mercator Ocean Journal*, 56, CMEMS
3 Special Issue, 2018.

4 Lin, J.G., Chiu, Y.F. and Weng W.K.: Wave forecast system of Hualien Harbour. In: Taiwan-
5 Polish Joint Seminar on Coastal Protection, 37-46, 2008.

6 Lorente, P., Piedracoba, S., Soto-Navarro, J. and Álvarez-Fanjul, E.: Accuracy assessment of
7 High Frequency radar current measurements in the Strait of Gibraltar, *Journal of Operational
8 Oceanography*, 7 (2), 59–73, 2014.

9 Lorente, P., Piedracoba, S., M.G. Sotillo, and Álvarez-Fanjul, E.: Long-term monitoring of the
10 Atlantic Jet through the Strait of Gibraltar with HF radar observations, *Journal of Marine
11 Science and Technology*, 6, 1-16, 2018.

12 Lyard, F., Lefevre, F., Letellier, T. and Francis, O.: Modelling the global ocean tides: modern
13 insights from FES2004, *Ocean Dynamics*, 56, 394-415, 2006.

14 Macias, D., García-Gorriz, E. and Stips, A.: The seasonal cycle of the Atlantic Jet dynamics in
15 the Alboran sea: direct atmospheric forcing versus Mediterranean thermohaline circulation,
16 *Ocean Dynamics*, 66, 137-151, doi: 10.1007/s10236-015-0914-y, 2016.

17 Macías, D., Martín, A.P., García-Lafuente, J., García, C.M., Yool, A., Bruno, M., Vázquez-
18 Escobar, A., Izquierdo, A., Sein, D.V. and Echevarría, F.: Analysis of mixing and
19 biogeochemical effects induced by tides on the Atlantic-Mediterranean flow in the Strait
20 of Gibraltar through a physical-biological coupled model, *Prog. Oceanogr.*, 74 (2-3), 252-
21 272, doi: 10.1016/j.pocean.2007.04.006, 2007a.

22 Macías, D., Navarro, G., Echevarría, F., Garcia C.M. and Cueto, J.L.: Phytoplankton pigment
23 distribution in the North-Western Alboran Sea and meteorological forcing: a remote
24 sensing study, *J. Mar. Res.*, 65, 523-543, 2007b.

25 Macías, D., Bruno, M., Echevarría, F., Vázquez, A. and Garcia C.M.: Meteorologically-induced
26 mesoscale variability of the North-Western Alboran sea (southern Spain) and related
27 biological patterns, *Estuar Coast Shelf Sci.*, 78, 250-266, 2008.

28 Madec G.: NEMO Ocean General Circulation Model, Reference Manual, Internal Report.
29 LODYC/IPSL, Paris, 2008.

30 Marshall, J., Hill, C., Perelman, L. and Adcroft, A.: Hydrostatic, quasi-hydrostatic, and
31 nonhydrostatic ocean modeling, *J. Geophys. Res.*, 102 (C3), 5733–5752, 1997.

32 McLaren, A., Fiedler, E., Roberts-Jones, J., Martin, M., Mao, C. and Good, S. QUALITY
33 INFORMATION DOCUMENT of Global Ocean OSTIA Near Real Time Level 4 Sea
34 Surface Temperature Product SST-GLO-SST-L4-NRT-OBSERVATIONS-010-001, freely
35 available in CMEMS website: <http://cmems-resources.cls.fr/documents/QUID/CMEMS-OSI-QUID-010-001.pdf>. Copernicus Marine Environment Monitoring Service, December
36 2016.

38 Mourre, B., Aguiar, E., Juza, M., Hernández-Lasheras, J., Reyes, E., Heslop, E., Escudier, R.,
39 Cutolo, E., Ruiz, S., Mason, E., Pascual, A. and Tintoré, J.: Assessment of high-resolution
40 regional ocean prediction systems using multi-platform observations: Illustrations in the
41 Western Mediterranean Sea. In “New Frontiers in operational Oceanography”. E.
42 Chassignet, A. Pascual, J. Tintoré and J. Verron, Eds., GODAE OceanView, 663-694,
43 doi:10.17125/gov2018.ch24, 2018.

1 O'Dea, E., Furner, R., Wakelin, S., Siddorn, J., While, J., Sykes, P., King, R., Holt, J., and
2 Hewitt, H.: The CO5 configuration of the 7 km Atlantic margin model: large-scale biases
3 and sensitivity to forcing, physics options and vertical resolution, *Geosci. Model Dev.*, 10,
4 2947-2969, 2017.

5 Otero, P., Ruiz-Villareal, M. and Peliz, A.: Variability of river plumes off Northwest Iberia in
6 response to wind events, *Journal of Marine Systems*, 72, 238-255, 2008.

7 Peliz, A., Rosa, T., Santos, A.M.P. and Pisarra, J.: Fronts, jets and counter flows in the Western
8 Iberian upwelling system, *Journal of Marine Systems*, 35 (1-2), 61-77, 2002.

9 Pérez, B., Álvarez-Fanjul, E, Pérez, S., de Alfonso, M. and Vela, J.: Use of tide-gauge data in
10 operational oceanography and sea level hazard warning systems. *Journal of Operational
11 Oceanography*, 6 (2), 1-18, 2013.

12 Pérez, B., Brouwer, R., Beckers, J., Paradis, D., Balseiro, C., Lyons, K., Cure, M., Sotillo, M.G.,
13 Hackett, B., Verlaan, M. and Fanjul, E.: ENSURF: multi-model sea level forecast:
14 implementation and validation results for the IBIROOS and Western Mediterranean regions,
15 *Ocean Sci.* 8 (2), 211–226, 2012.

16 Pingree, R. and Le Cann, B.: Three anticyclonic slope water eddies (swoddies) in the southern
17 bay of Biscay in 1990, *Deep Sea Res, Part A*, 39, 1147–1175, 1992.

18 Reyes, E.: A high-resolution modeling study of the ocean response to wind forcing within the
19 Strait of Gibraltar, Phd. Dissertation, University of Cadiz, Spain, 2015.

20 Rockel, B.: The regional downscaling approach: a brief history and recent advances, *Curr Clim
21 Change Rep.*, 1, 22-29, doi: 10.1007/s40641-014-0001-3, 2015.

22 Ruiz, J., Macias, D., Rincón, M., Pascual, A., Catalan, I.A. and Navarro, G.: Recruiting at the
23 edge: kinetic energy inhibits anchovy populations in the Western Mediterranean, *Plos One*
24 8 (2), e55523, doi: 10.1371/journal.pone.0055523, 2013.

25 Sánchez-Arcilla, A., Sierra, J.P., Brown, S., Casas-Prat, M., Nicholls, R.J., Lionello, P. and
26 Conte, D.: A review of potential physical impacts on harbours in the Mediterranean Sea
27 under climate change, *Regional Environmental Change*, 16, 2471-2484, 2016.

28 Sánchez-Garrido, J.C., Sannino, G., Liberti, L., García Lafuente, J. and Pratt, L.: Numerical
29 Modeling of three-dimensional stratified tidal flow over Camarinal Sill, Strait of Gibraltar.
30 *Journal of Geophysical Research*, 116, C12026, doi: 10.1029/2011JC007093, 2011.

31 Sánchez-Garrido, J.C., García-Lafuente, J., Álvarez-Fanjul, E., Sotillo, M.G. and De los Santos
32 F.J.: What does cause the collapse of the Western Alboran Gyre? Results of an operational
33 ocean circulation system, *Progress in Oceanography*, 116, 142–153, 2013.

34 Sánchez-Garrido, J.C., García-Lafuente, J., Sammartino, S., Naranjo, C., De los Santos, F.J.
35 and Álvarez-Fanjul, E.: Meteorologically-driven circulation and flushing times of the Bay
36 of Algeciras, Strait of Gibraltar, *Marine Pollution Bulletin*, 80, 97-106, 2014.

37 Sánchez-Garrido, J.C., Naranjo, C., Macías, D., García-Lafuente, J. and Oguz T.: Modeling the
38 impact of tidal flows on the biological productivity of the Alboran Sea, *J. Geophys. Res:
39 Oceans*, 120, 7329-7345, 2015.

40 Sannino, G., Bargagli, A. and Artale, V.: Numerical modeling of the semidiurnal tidal exchange
41 through the Strait of Gibraltar, *J. Geophys. Res.*, 109, C05011, doi:10.1029/2003JC002057,
42 2004.

1 Sammartino, S., García-Lafuente, J., Sánchez-Garrido, J.C., De los Santos, F.J., Álvarez-
2 Fanjul, E., Naranjo, C., Bruno, M. and Calero-Quesada, C.: A numerical model analysis of
3 the tidal flows in the Bay of Algeciras, Strait of Gibraltar, Continental Shelf Research, 72,
4 34–46, doi:10.1016/j.csr.2013.11.002, 2014.

5 Sammartino, S., Sánchez Garrido, J.C., Naranjo, C., García-Lafuente, J., Rodríguez Rubio, P.
6 and Sotillo, M.G.: Water renewal in semi-enclosed basins: A high resolution Lagrangian
7 approach with application to the Bay of Algeciras, Strait of Gibraltar, Limnol. Oceanogr.
8 Methods, 16, 106-118, doi:10.1002/lom3.10231, 2018.

9 Saux-Pickart, E., Orain, F. and Roquet, H. QUALITY INFORMATION DOCUMENT of
10 European Near Real Time Level 3S Sea Surface Temperature Product
11 SST_EUR_L3S_NRT_OBSERVATIONS_010_009_a, freely available in CMEMS website
12 <http://resources.marine.copernicus.eu/documents/QUID/CMEMS-SST-QUID-010-009-a.pdf>. Copernicus Marine Environment Monitoring Service, March 2019.

14 Simpson, J.H.: Physical processes in the ROFI regime, Journal of Marine Systems, 12 (1), 3-
15 15, 1997.

16 Solé, J., Ballabrera-Poy, J., Macias, D. and Catalán, I.A.: The role of ocean velocity in
17 chlorophyll variability, a modelling study in the Alboran Sea, Scientia Marina, 80 (S1), 249-
18 256, 2016.

19 Sotillo, M.G., Cailleau, S., Lorente, P., Levier, B., Aznar, R., Reffray, G., Amo-Baladrón, A.
20 and Álvarez-Fanjul, E.: The MyOcean IBI Ocean Forecast and Reanalysis Systems:
21 Operational products and roadmap to the future Copernicus Service, Journal of Operational
22 Oceanography, 8 (1), 1-18, 2015.

23 Sotillo M.G., Amo-Baladrón, A., Padorno, E., García-Ladona, E., Orfila, A., Rodríguez-Rubio,
24 P., Conte, D., Jiménez J.A., De los Santos, F.J. and Álvarez-Fanjul, E.: How is the surface
25 Atlantic water inflow through the Strait of Gibraltar forecasted? A lagrangian validation of
26 operational oceanographic services in the Alboran Sea and Western Mediterranean, Deep
27 Sea Research, 133, 100-117, 2016-a.

28 Sotillo M.G., García-Ladona, E., Orfila, A., Rodríguez-Rubio, P., Maraver J.C., Conti, D.,
29 Padorno, E., Jiménez J.A., Capó, E., Pérez, F., Sayol, J.M., De los Santos, F.J., Amo-
30 Baladrón, A., Rietz, A., Troupin, C., Tintoré, J. and Álvarez-Fanjul, E.: The MEDESS.GIB
31 database: tracking the Atlantic water inflow, Earth Syst. Sci. Data, 8, 141-149, 2016-b.

32 Soto-Navarro, J., Lorente, P., Álvarez-Fanjul, E., Sánchez-Garrido, J.C. and García-Lafuente,
33 J.: Surface circulation at the Strait of Gibraltar: a combined HF radar and high resolution
34 model study, Journal of Geophysical Research, Oceans, 121, doi:10.1002/2015jc011354,
35 2016.

36 Stanev, E.V., Ziemer, F., Schultz-Stellenfleth, J., Seemann, J., Staneva, J. and Gurgel, K.W.:
37 Blending Surface Currents from HF Radar Observations and Numerical Modelling: Tidal
38 Hindcasts and Forecasts, Journal of Atmospheric and Oceanic Technology, 32, 256-281,
39 2015.

40 Stanev, E.V., Schulz-Stellenfleth, J., Staneva, J., Grayek, S., Grashorn, S., Behrens, A., Koch,
41 W. and Pein, J.: Ocean forecasting for the German Bight: from regional to coastal scales,
42 Ocean Science, 12, 1105-1136, doi: 10.5194/os-12-1105-2016, 2016.

1 Stanev, E.V., Grashorn, S. and Zhang, Y.J.: Cascading ocean basins: numerical simulations of
2 the circulation and interbasin exchange in the Azov - Black - Marmara - Mediterranean Seas
3 system. *Ocean Dynamics*, 67, 1003–1025, 2017.

4 Stobart, B., Mayfield, S., Mundy, C., Hobday, A., and Hartog, J.: Comparison of in situ and
5 satellite sea surface-temperature data from South Australia and Tasmania: how reliable are
6 satellite data as a proxy for coastal temperatures in temperate southern Australia? *Mar.*
7 *Freshw. Res.* 67, 612–625. doi: 10.1071/MF14340, 2015.

8 Thakur, K.K., Varderstichel, R., Barrel, J., Stryhn, H., Patanasatienkul, T. and Revie, C.W.:
9 Comparison of remotely-sensed sea surface temperature and salinity products with in situ
10 measurements from British Columbia, Canada. *Frontiers in Marine Science*,
11 doi:10.3389/fmars.2018.00121, 2018.

12 Vandenbulcke, L., Beckers, J.M. and Barth, A.: Correction of inertial oscillations by
13 assimilation of HF radar data in a model of the Ligurian Sea, *Ocean Dynamics*, 67, 117,
14 <https://doi.org/10.1007/s10236-016-1012-5>, 2017.

15 Vargas-Yáñez, M., Plaza, F., García-Lafuente, J., Sarhan, T., Vargas, J.M. and Vélez-Belchí,
16 P.: About the seasonal variability of the Alboran Sea circulation, *Journal of Marine*
17 *Systems*, 35, 229-248, 2002.

18 Viúdez, A.: An explanation for the curvature of the Atlantic Jet past the Strait of Gibraltar,
19 *Journal of Physical Oceanography*, 27, 1804-1810, 1997.

20 Viúdez, A., Pinot, J.M. and Harney, R.L.: On the upper layer circulation in the Alboran Sea,
21 *Journal of Geophysical Research*, 103 (C10), 21653-21666, 1998.

22 Wilkin, J., Rosenfeld, L., Allen, A., Baltes, R., Baptista, A., He, R., Hogan, P., Kurapov, A.,
23 Mehra, A., Quintrell, J., Schwab, D., Signell, R. and Smith, J.: Advancing coastal ocean
24 modelling, analysis, and prediction for the US Integrated Ocean Observing System. *Journal*
25 *of Operational Oceanography*, 10 (2), 115–126, 2017.

26 Zhang, Y.J., Stanev, E.V. and Grashorn, S.: Unstructured-grid model for the North Sea and
27 Baltic Sea: validation against observations. *Ocean Modelling*, 97, 91–108, 2016.

28

29

30

31

32

33

34

35

36

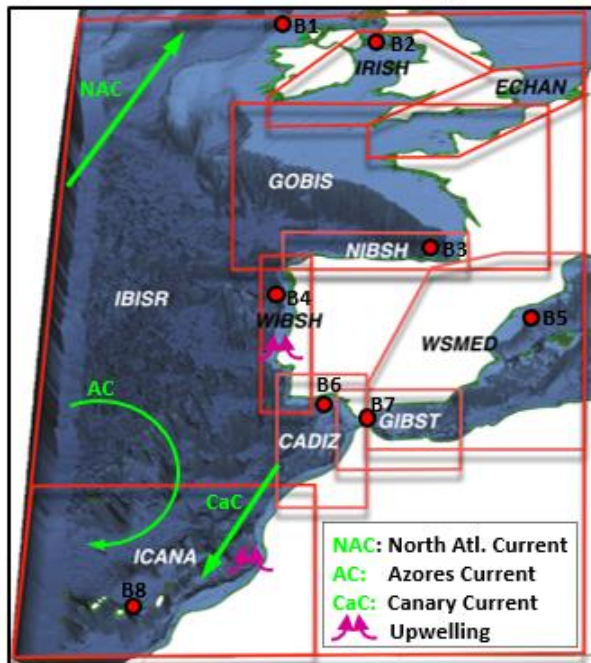
37

38

39

40

1 a) IBI Service -IBISR- domain and subregions



b) SAMPA model domain: GIBST

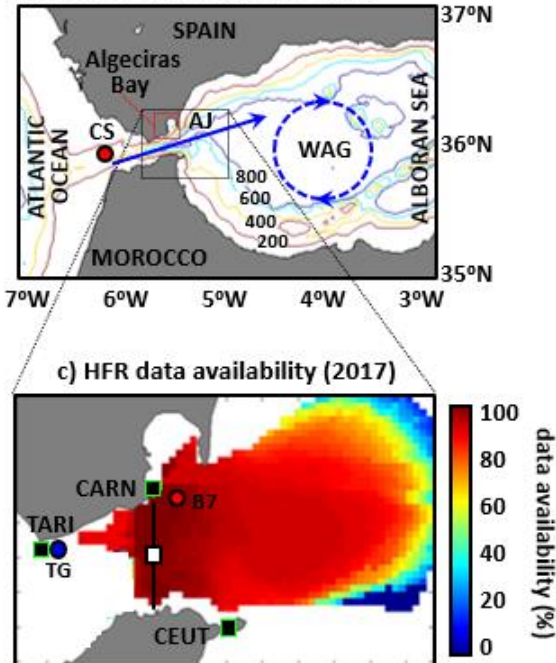
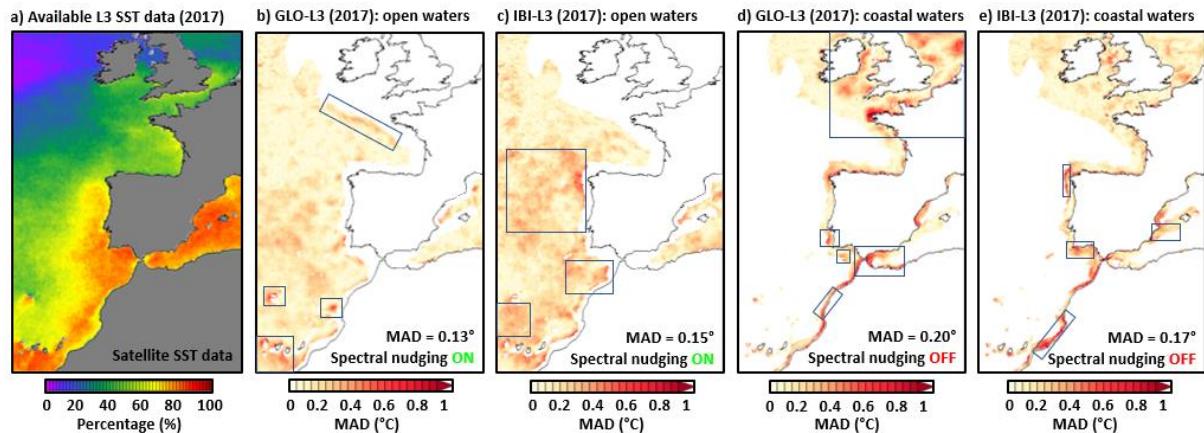


Figure 1. a) Iberia-Biscay-Ireland Service (IBISR) domain, which comprises 9 sub-regions denoted by red squares. Red filled dots represent buoy locations. b) Study area: coverage domain of SAMPA coastal ocean model, where the surface Atlantic Jet (AJ) flows through the Strait of Gibraltar into the Alboran Sea, feeding the Western Alboran Gyre (WAG); isobath depths are labeled every 200 m. Red dot indicates a topographic feature: Camarinal Sill (CS). c) HFR hourly data availability for 2017: solid black squares represent radar sites, blue and red dots indicate Tarifa tide-gauge and B7 buoy location, respectively. The black line denotes the selected transect and the white square represents its midpoint.

1



2

3 Figure 2. a) Availability of satellite-derived L3 SST daily data for 2017; b-c) Annual Mean
 4 Absolute Difference (MAD) of SST for 2017 in open waters where the spectral nudging is
 5 applied: GLOBAL versus satellite and IBI versus satellite; d-e) Idem but in coastal waters
 6 where no spectral nudging is applied. Zones of worse model performance (i.e., higher MAD)
 7 are delimited with blue rectangles. Spatially-averaged MAD values are provided in the lower
 8 right corner.

9

10

11

12

13

14

15

16

17

18

19

20

21

22

23

24

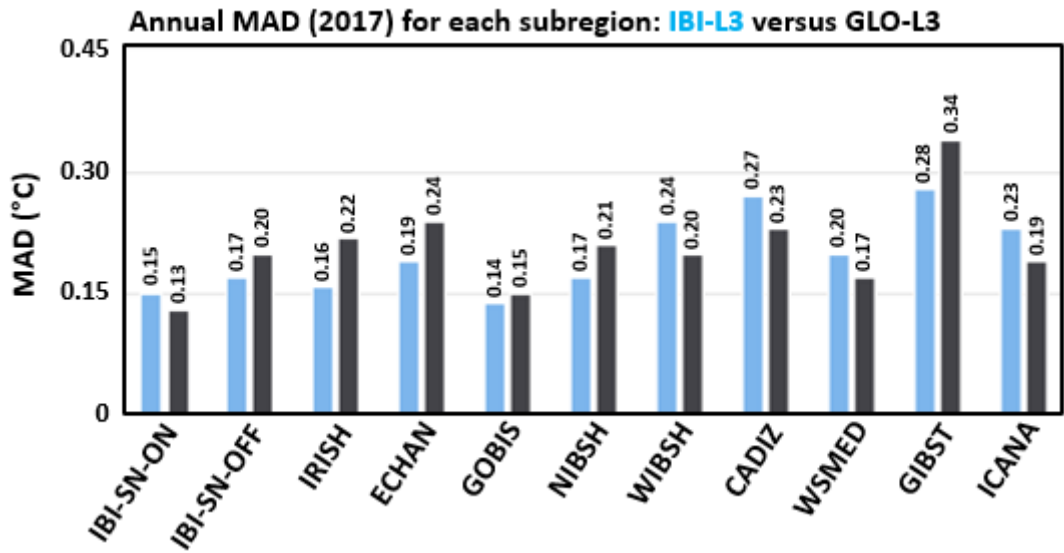
25

26

27

28

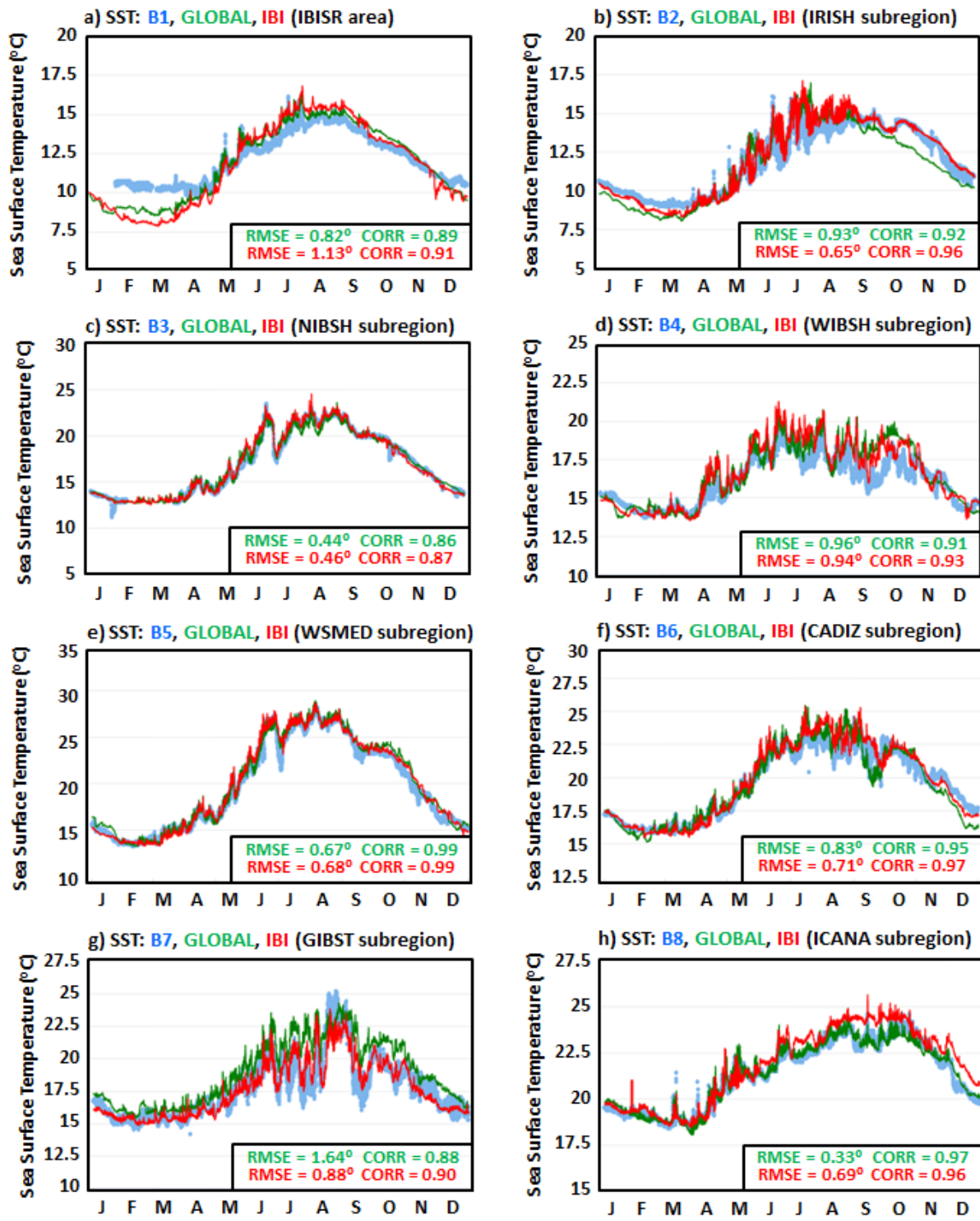
1



2

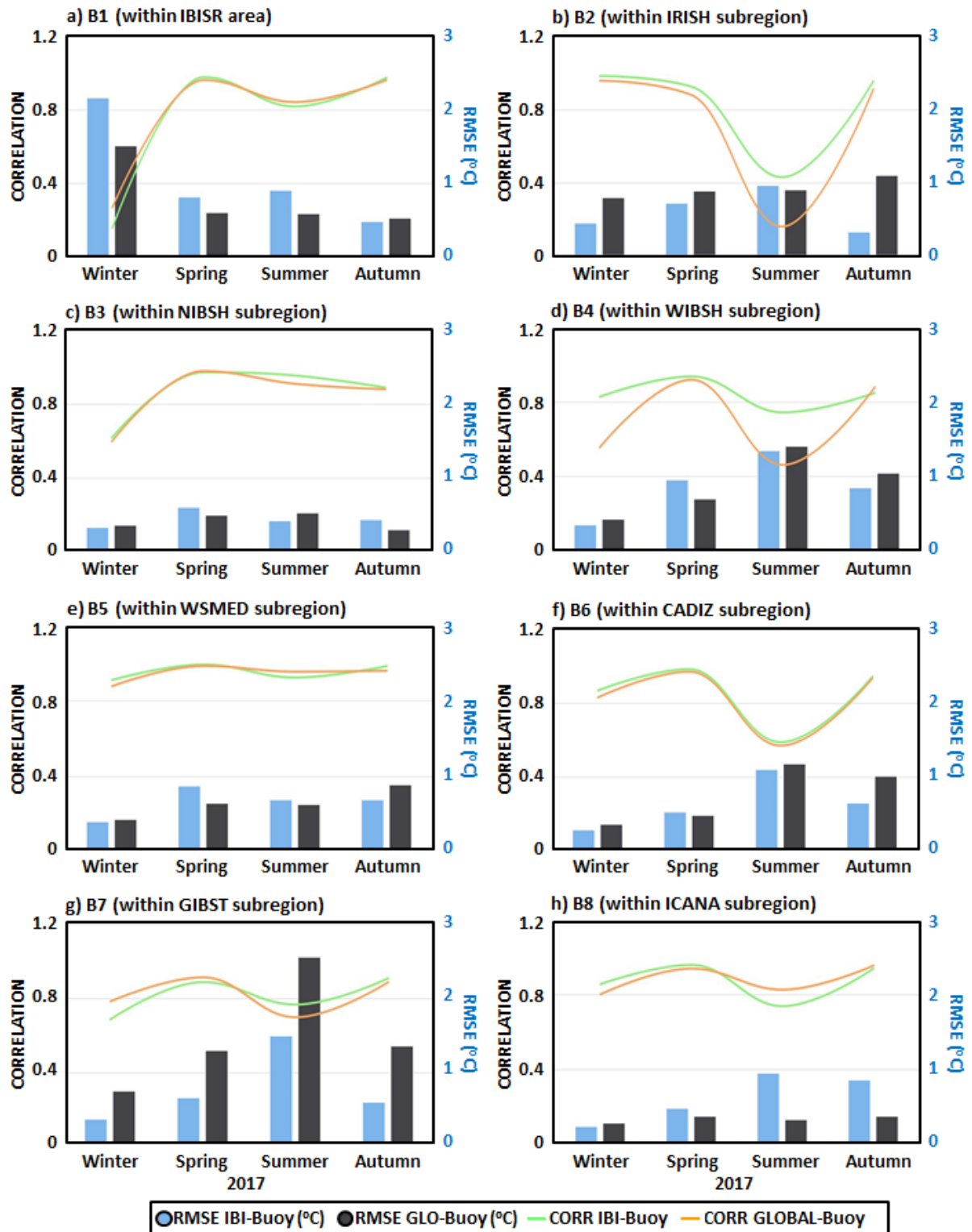
3 Figure 3. Annual (2017) Mean Absolute difference (MAD) of SST, spatially-averaged for each
4 sub-region (defined in Figure 1-a), between IBI (GLOBAL) and satellite L3 observations,
5 represented by blue (black) columns. IBI-SN-ON (IBI-SN-OFF) represents the area where the
6 spectral nudging technique was (was not) applied.

7



1
2 Figure 4. Annual (2017) time series of hourly Sea Surface Temperature (SST) at eight different
3 locations within IBISR area. In situ observations from moored buoys (blue dots), GLOBAL
4 model predictions (green line) and IBI model outputs (red line) are depicted. Skill metrics
5 derived from model-observation comparison are gathered in black boxes.
6
7
8

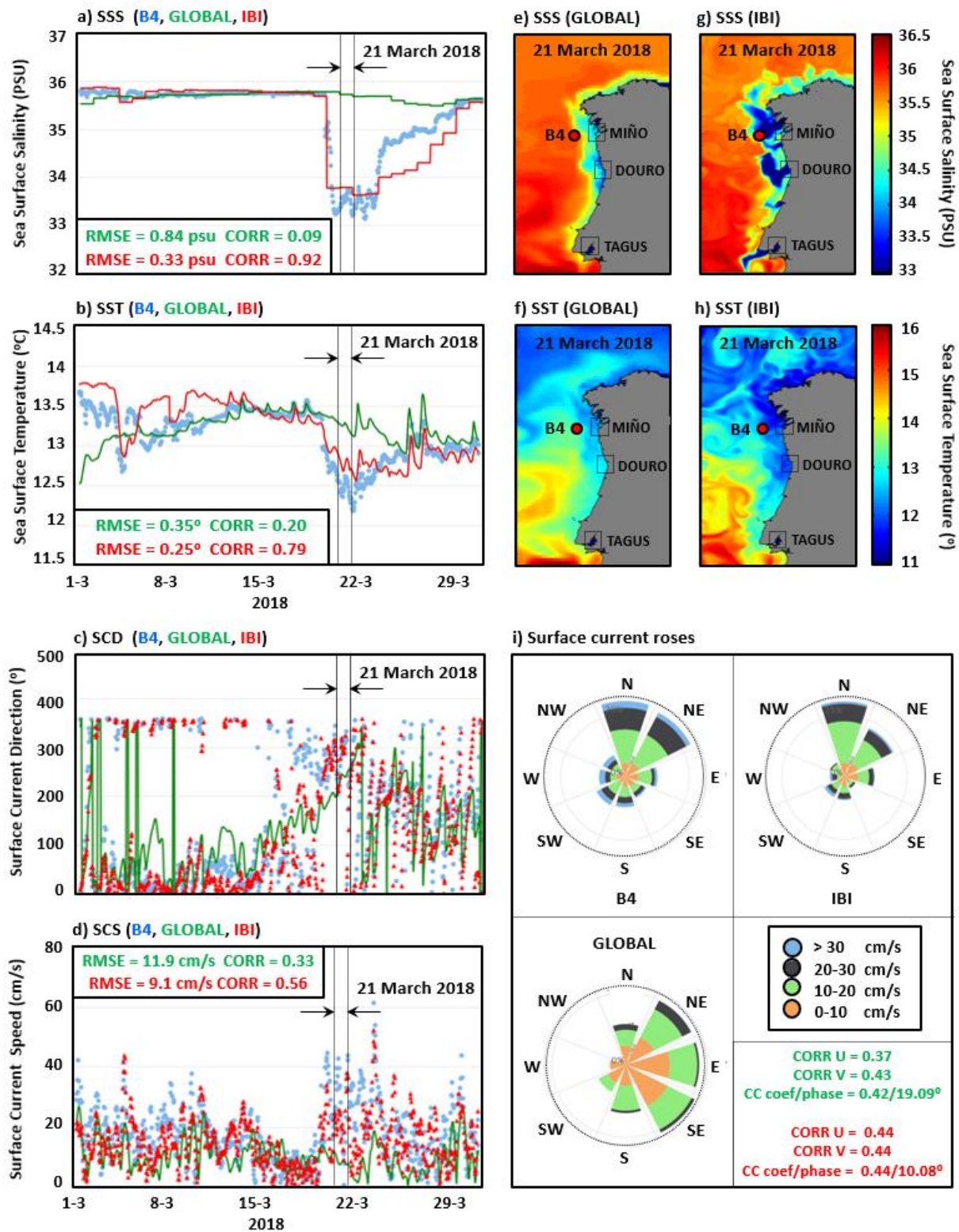
1



2

3 Figure 5. Annual evolution (2017) of seasonal skill metrics derived from the comparison of
4 GLOBAL and IBI models against in situ SST hourly observations provided by eight buoys.
5 RMSD and correlation coefficient represented by coloured bars and lines, respectively.

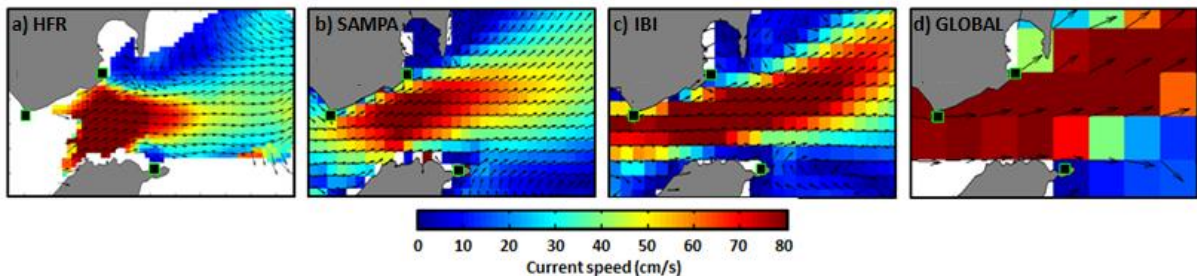
6



1

2 Figure 6. (a-d) Monthly inter-comparison (March 2018) between GLOBAL (green line), IBI
 3 (red line / red triangles) and B4 buoy (blue dots): sea surface salinity (SSS), temperature (SST),
 4 current direction (SCD) and current speed (SCS); (e-f) Daily maps of SSS and SST derived
 5 from GLOBAL outputs for the 21st of March. Red filled dot represents B4 buoy location; (g-h)
 6 Daily maps of SSS and SST derived from IBI outputs for the 21st of March; (i) Monthly surface
 7 current roses. Monthly skill metrics derived from model-observation comparisons are provided.

1



2

3 Figure 7. Annual mean circulation pattern in GIBST for 2017, derived from hourly estimations
4 provided by: a) HFR; b) SAMPA coastal model; c) IBI regional model; d) GLOBAL model.
5 For the sake of clarity, only one vector every two was plotted in HFR map.

6

7

8

9

10

11

12

13

14

15

16

17

18

19

20

21

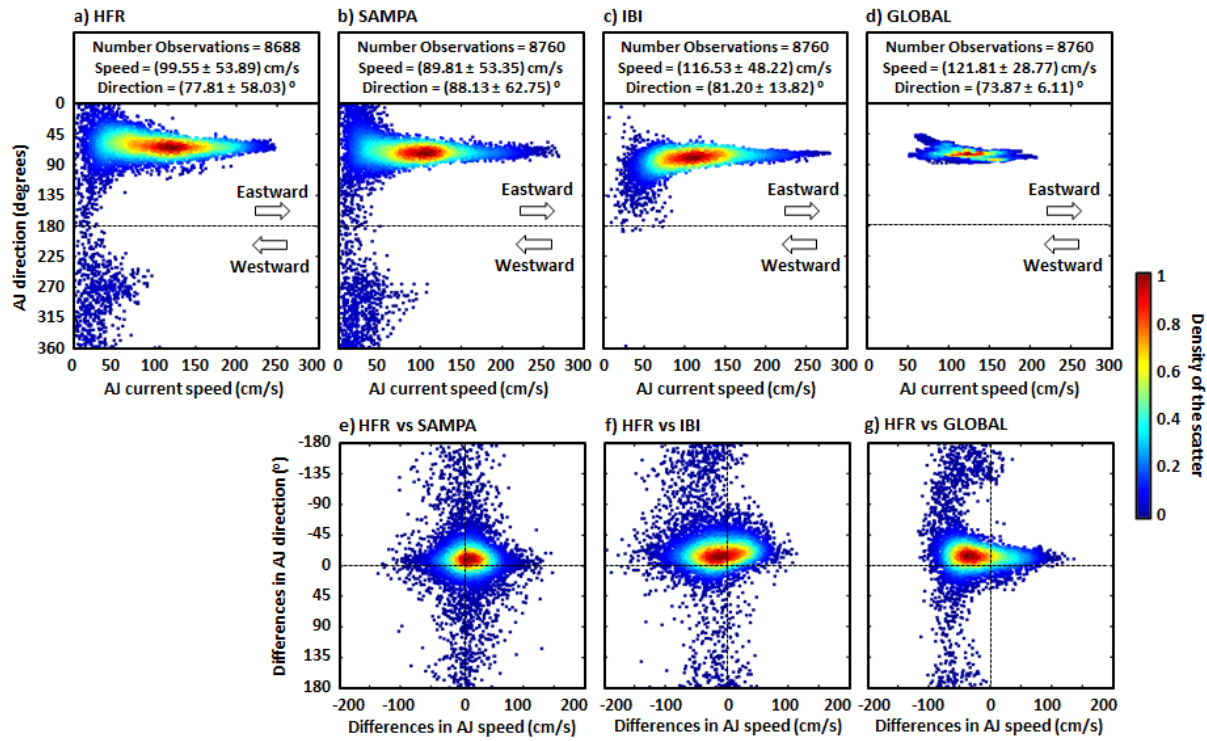
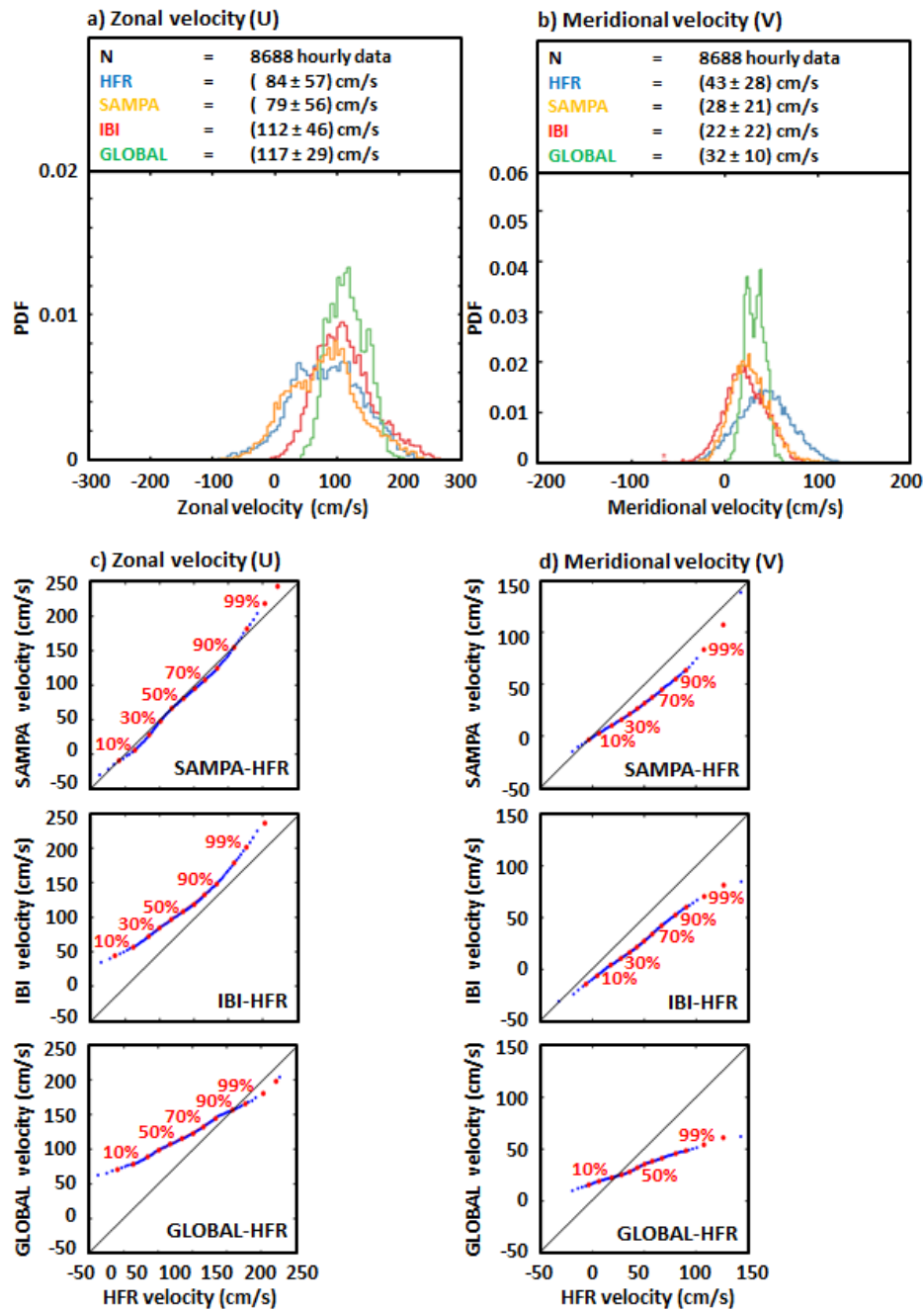


Figure 8. (a-d) Annual (2017) scatter plot of hourly AJ current speed versus direction (angle measured clockwise from the North); estimations provided by: a) HFR; b) SAMPA; c) IBI; d) GLOBAL. Mean and standard deviation values of both AJ speed and direction are gathered in black boxes; (e-g) Annual scatter plot of differences (observation minus model) in AJ speed and direction between: e) HFR and SAMPA; f) HFR and IBI; g) HFR and GLOBAL.

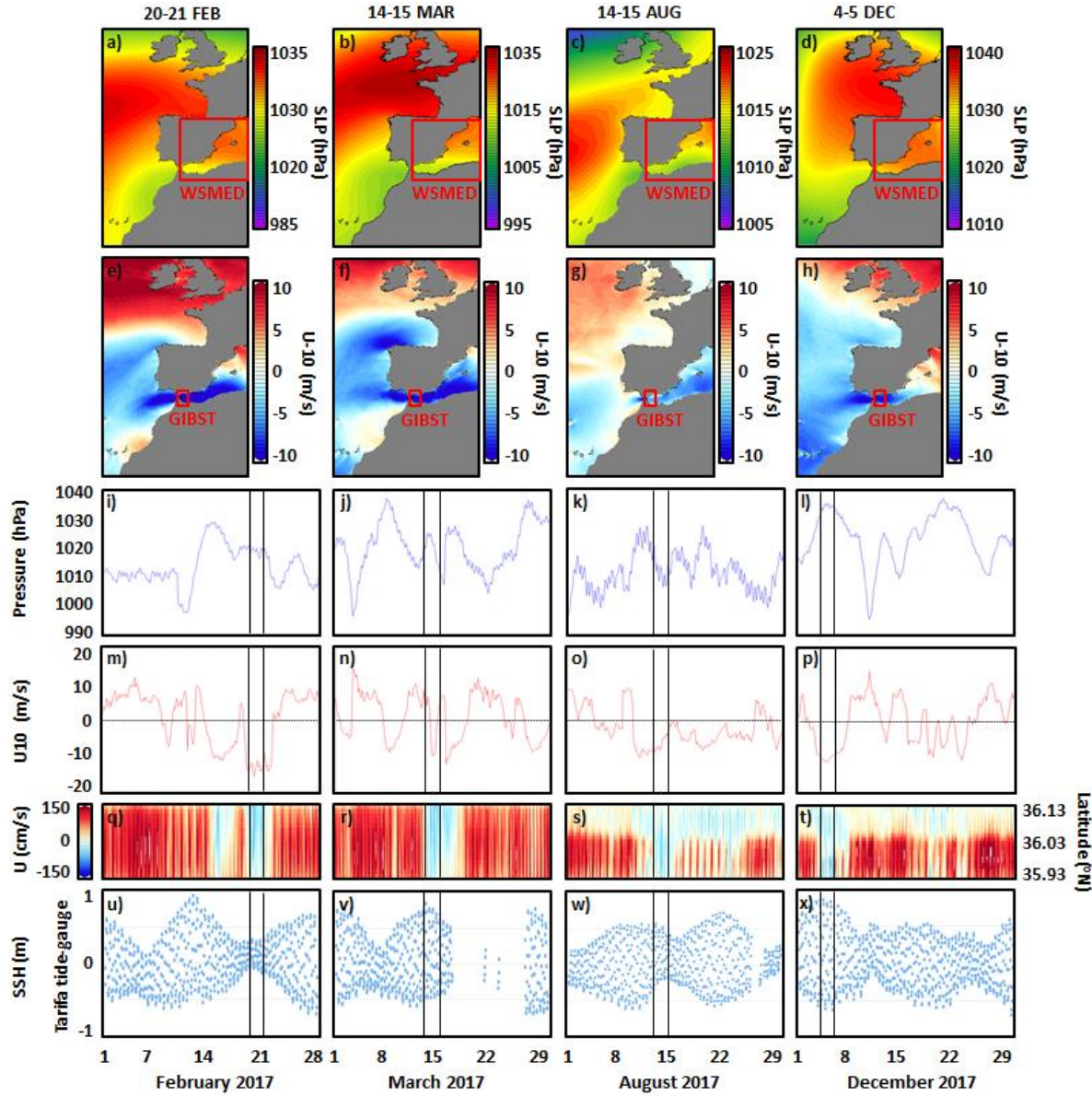
1
2
3
4



6 Figure 9. Annual (2017) histogram of hourly: (a) zonal current velocities; (b) meridional current
7 velocities, as provided by HFR, SAMPA, IBI and GLOBAL. Mean and standard deviation
8 values are gathered in black boxes. Quantile-quantile plots of hourly: (c) zonal current
9 velocities; (d) meridional current velocities, as derived from the observation-model
10 comparison. 10–99% quantiles were established (red filled dots);

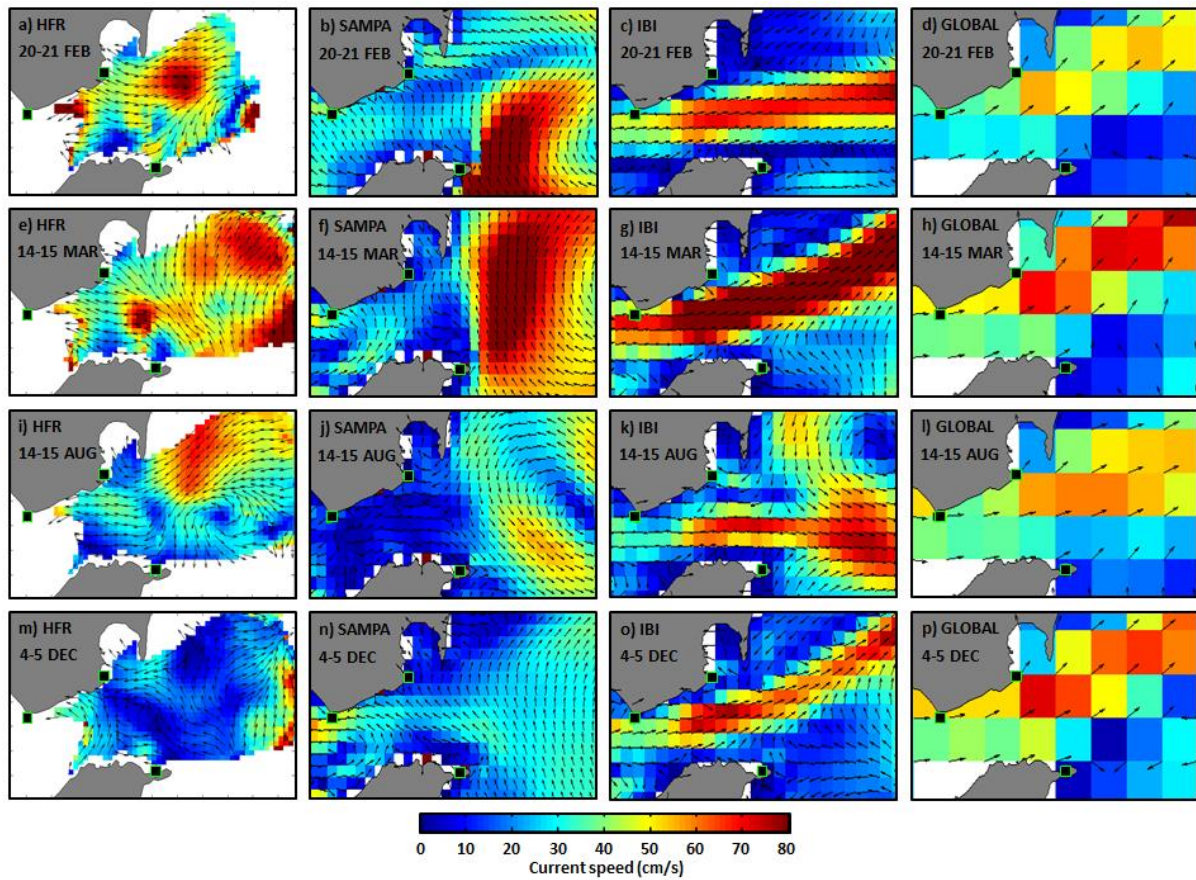
11

1



2

3 Figure 10. 2-day averaged synoptic maps of: (a-d) sea level pressure (SLP); (e-h) zonal wind
 4 at 10 m height (U-10), provided by ECMWF, corresponding to each of the four Atlantic inflow
 5 reversal events analysed during 2017. (i-l) Monthly time series of SLP, spatially averaged over
 6 the Western Mediterranean (WSMED) subregion, marked with a big red box in the maps of the
 7 first row; (m-p) Monthly time series of U-10, spatially averaged over the Strait of Gibraltar
 8 (GIBST) subregion, marked with a small red box in the maps of the second row; (q-t) Monthly
 9 Hovmöller diagrams of HFR-derived zonal current velocity at the selected transect. Red (blue)
 10 colour represent eastward (westward) flow; (u-x) Monthly time series of hourly sea surface
 11 height (SSH) provided by Tarifa tide-gauge, represented by a blue dot in Figure 1-c. 2-day
 12 episodes of permanent flow reversal are marked with black boxes in (i-x).



1
2 Figure 11. 2-day averaged maps of the surface circulation in GIBST, corresponding to each of
3 the four Atlantic inflow reversal events detected in 2017 (from top to bottom). Maps derived
4 from hourly estimations were provided by (from left to right): HFR, SAMPA coastal model,
5 IBI regional model and GLOBAL model. For the sake of clarity, only one vector every two was
6 plotted in HFR map.

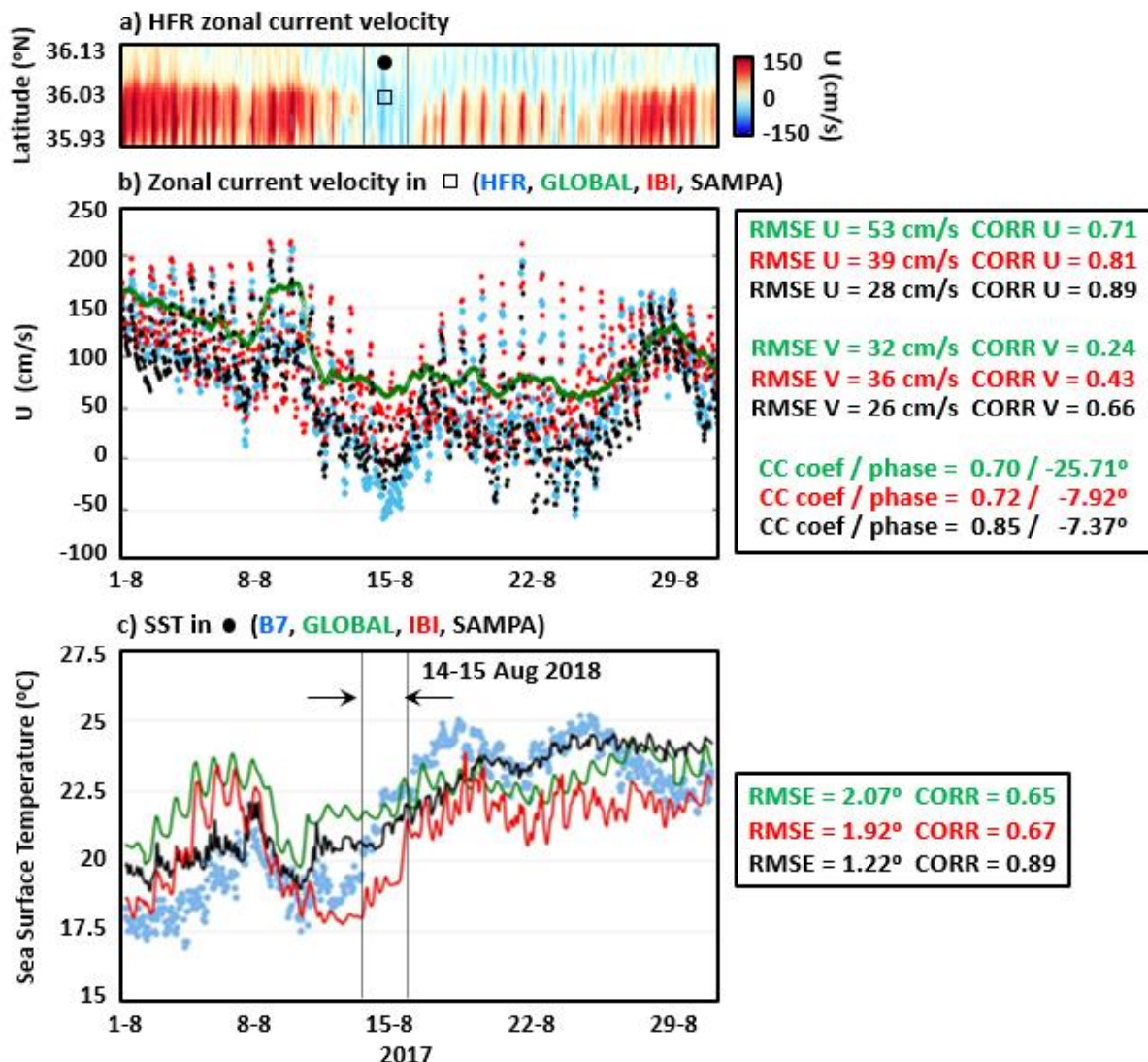


Figure 12. a) Monthly Hovmöller diagram of HFR-derived zonal current velocity at the selected transect in the Strait of Gibraltar for August 2017. Red (blue) colour represent eastward (westward) flow. A complete Atlantic inflow reversal episode marked with black box for the 14-15 August; b) Monthly times series of zonal current velocity at the midpoint of the transect (represented by a black square in the Hovmöller diagram) provided by HFR (blue dots), SAMPA (black dots), IBI (red dots) and GLOBAL (green dots); c) Monthly time series of SST provided by B7 buoy (blue dots), SAMPA (black line), IBI (red line) and GLOBAL (green line). Monthly skill metrics derived from observation-model comparison are gathered in black boxes on the right.

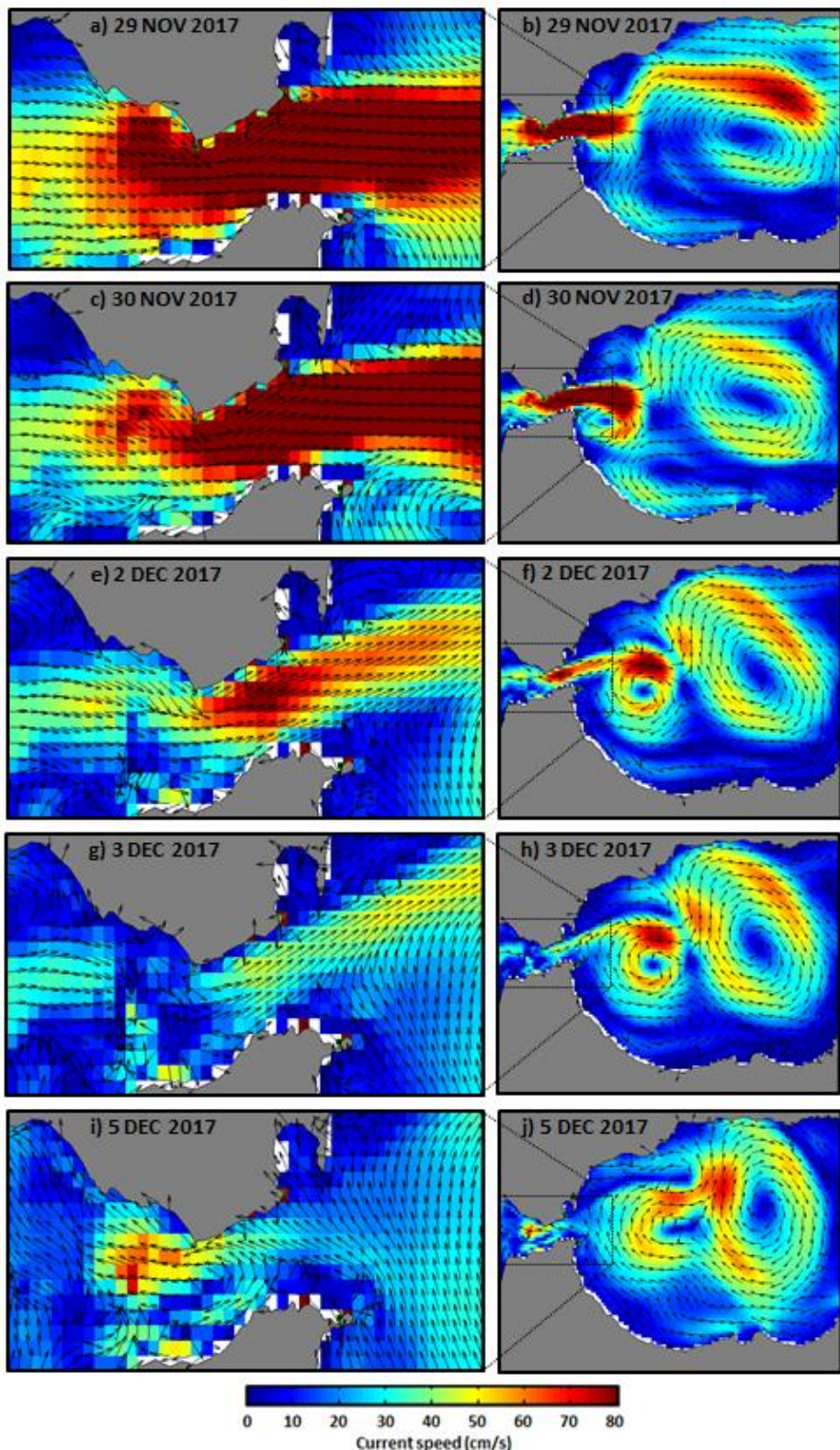


Figure 13. Sequence of SAMPA daily surface circulation maps covering the period from the 29th of November to the 5th of December 2017. General map on the right and zoom over the Strait of Gibraltar on the left. An inflow reversal through the narrowest section of the Strait of Gibraltar is evidenced by the 5th of December, as a result of a change in the wind regime, from westerlies to easterlies.

1

Features \ Model	CMEMS GLOBAL	CMEMS IBI	SAMPA
Model	NEMO 3.1	NEMO 3.6	MITgcm
Configuration	Global	Regional	Coastal
Domain: lon, lat	180°W-180°E, 89°S-90°N	19°W-5°E, 26°N-56°N	7.4°W-3°W, 35°N-37.2°N
Resolution	1/12°	1/36°	Variable (300-500 m at GIBST)
Product grid points	4320 x 2041	865 x 1081	200 x 100
Forecast (days)	10	5	3
Forecast update	Daily	Daily	Daily
Depth levels	50 (unevenly distributed)	50 (unevenly distributed)	46 (unevenly distributed)
Initial conditions	EN4 climatology	GLOBAL	IBI + NIVMAR
Open boundary conditions	NO	Daily 3D data from CMEMS GLOBAL	Daily 3D data from CMEMS IBI + barotropic velocity from NIVMAR+ tidal forcing from Mog2D model
Atmospheric forcing	ECMWF (3-h)	ECMWF (3-h)	AEMET (1-h)
Rivers forcing	Monthly climatology	Climatology + Previmer + SMHI	NO
Tidal forcing	NO	11 tidal harmonics from FES2004 and TPXO7.1 models	8 tidal harmonics from FES2004 (Mog2D model)
Assimilation	YES (SAM2)	NO*	NO
Bathymetry	ETOPO1 + GEBCO8	ETOPO1 + GEBCO8	IOC + high resolution charts

2 Table 1. Basic features of the ocean forecast systems employed in the present study. * The
 3 operational version of IBI here used with spectral nudging. Assimilation scheme SAM2 was
 4 later introduced in v4 (April 2018).

5

6

7

8

9

1
2

Buoy	Model	Year	Location: lon, lat	Subregion	Depth (m)	Sampling
B1	WaveScan	2008	9.07°W, 54.67°N	IBISR	72	1 h
B2	WaveScan	2008	5.42°W, 53.47°N	IRISH	95	1 h
B3	SeaWatch	1990	3.09°W, 43.64°N	NIBSH	870	1 h
B4	SeaWatch	1998	9.43°W, 42.12°N	WIBSH	600	1 h
B5	SeaWatch	2004	1.47°E, 40.68°N	WSMED	688	1 h
B6	SeaWatch	1996	6.96°W, 36.48°N	CADIZ	450	1 h
B7	WatchKeeper	2010	5.42°W, 36.07°N	GIBST	40	1 h
B8	Triaxys	1992	15.39°W, 28.05°N	ICANA	30	1 h

3 Table 2. Description of the network of directional buoys used in this work. Year label stands
4 for year of deployment. Subregions are defined in Figure 1-a.

5
6

Metrics \ HFR vs:	GLOBAL	IBI	SAMPA
Bias U (cm·s⁻¹)	-32.98	-28.25	4.17
RMSD U (cm·s⁻¹)	52.89	50.89	33.58
CORR U	0.71	0.68	0.83
Slope U	0.37	0.55	0.82
Intercept U (cm·s⁻¹)	85.93	65.46	10.77
Bias V (cm/s)	10.52	20.32	15.19
RMSD V (cm·s⁻¹)	30.57	36.09	28.48
CORR V	0.15	0.33	0.56
Slope V	0.05	0.26	0.41
Intercept V (cm·s⁻¹)	29.98	11.27	10.17
Complex CORR	0.67	0.62	0.79
Phase (°)	-22.72	-12.68	-7.86

7
8
9
10

Table 3. Skill metrics derived from the 1-year (2017) validation of sea surface currents
estimated by three operational forecasting systems against HFR-derived observations at the
midpoint of the selected transect in the Strait of Gibraltar (Figure 1, c).

11